Available online at www.sciencedirect.com
ScienceDirect
Journal of Computational Physics 226 (2007) 509–533
JOURNAL OF COMPUTATIONAL PHYSICS
www.elsevier.com/locate/jcp

PHOENIX: MHD spectral code for rotating laboratory and gravitating astrophysical plasmas

J.W.S. Blokland [a,*], B. van der Holst [b], R. Keppens [a,b,c], J.P. Goedbloed [a,c]

[a] *FOM-Institute for Plasma Physics 'Rijnhuizen', Association Euratom-FOM, Trilateral Euregio Cluster, P.O. Box 1207, 3430 BE Nieuwegein, The Netherlands*
[b] *Centre for Plasma Astrophysics, K.U. Leuven, Belgium*
[c] *Astronomical Institute, Utrecht University, The Netherlands*

Received 26 September 2006; received in revised form 19 March 2007; accepted 20 April 2007
Available online 1 May 2007

Abstract

The new PHOENIX code is discussed together with a sample of many new results that are obtained concerning magnetohydrodynamic (MHD) spectra of axisymmetric plasmas where flow and gravity are consistently taken into account. PHOENIX, developed from the CASTOR code [W. Kerner, J.P. Goedbloed, G.T.A. Huysmans, S. Poedts, E. Schwarz, J. Comput. Phys. 142 (1998) 271], incorporates purely toroidal, or both toroidal and poloidal flow and external gravitational fields to compute the entire ideal or resistive MHD spectrum for general tokamak or accretion disk configurations. These equilibria are computed by means of FINESSE [A.J.C. Beliën, M.A. Botchev, J.P. Goedbloed, B. van der Holst, R. Keppens, J. Comp. Physics 182 (2002) 91], which discriminates between the different elliptic flow regimes that may occur. PHOENIX makes use of a finite element method in combination with a spectral method for the discretization. This leads to a large generalized eigenvalue problem, which is solved by means of Jacobi–Davidson algorithm [G.L.G. Sleijpen, H.A. van der Vorst, SIAM J. Matrix Anal. Appl. 17 (1996) 401].

PHOENIX is compared with CASTOR, PEST-1 and ERATO for an internal mode of Soloviev equilibria. Furthermore, the resistive internal kink mode has been computed to demonstrate that the code can accurately handle small values for the resistivity. A new reference test case for a Soloviev-like equilibrium with toroidal flow shows that, on a particular unstable mode, the flow has a quantifiable stabilizing effect regardless of the direction of the flow. PHOENIX reproduces the Toroidal Flow induced Alfvén Eigenmode (TFAE, [B. van der Holst, A.J.C. Beliën, J.P. Goedbloed, Phys. Rev. Lett. 84 (2000) 2865]) where finite resistivity in combination with equilibrium flow effects causes resonant damping. Localized ideal gap modes are presented for tokamak plasmas with toroidal and poloidal flow. Finally, we demonstrate the ability to spectrally diagnose magnetized accretion disk equilibria where gravity acts together with either purely toroidal flow or both toroidal and poloidal flow. These cases show that the MHD continua can be unstable or overstable due to the presence of a gravitational field together with equilibrium flow-driven dynamics [J.P. Goedbloed, A.J.C. Beliën, B. van der Holst, R. Keppens, Phys. Plasmas 11 (2004) 28].

* Corresponding author. Tel.: +31 (0)30 609 6839.
E-mail addresses: J-W.S.Blokland@Rijnhuizen.nl (J.W.S. Blokland), Bart.vanderHolst@wis.kuleuven.be (B. van der Holst), Rony.Keppens@wis.kuleuven.be (R. Keppens), Goedbloed@Rijnhuizen.nl (J.P. Goedbloed).
URLs: http://www.rijnh.nl (J.W.S. Blokland), http://www.rijnh.nl (R. Keppens), http://www.rijnh.nl (J.P. Goedbloed).

0021-9991/$ - see front matter © 2007 Elsevier Inc. All rights reserved.
doi:10.1016/j.jcp.2007.04.018

Keywords: Magnetohydrodynamics; Resistive; Spectrum; Tokamak; Accretion disk; Stability

1. Introduction

In current tokamak experiments, plasma flows play an ever more important role for the determination of plasma equilibrium, stability and transport properties. The flows induced by neutral beam injection are mainly in the toroidal direction. Recently, there are indications that the plasma also rotates in the poloidal direction, see for example Crombé et al. [10] and Busch et al. [7]. In an astrophysical accretion torus or disk, the plasma rotates in the toroidal direction but also experiences the influence of an external gravitational field caused by the central accreting object, like a young stellar object, neutron star or black hole. To investigate the stability properties of tokamak or accretion disk plasmas, flow and gravity have to be taken into account in both the equilibrium and the stability studies.

Computing equilibria and stability of rotating plasmas becomes a real tour de force when the poloidal flow velocity is not restricted to small values since the different characteristic MHD speeds give rise to "transsonic" flow transitions when the stationary equilibria change from elliptic to hyperbolic, or vica versa. In general, stationary equilibrium solvers break down in the hyperbolic flow regimes and we may even question whether the whole scheme of distinguishing between equilibrium and perturbation makes sense there (Goedbloed [14,15]). In the recently developed equilibrium code FINESSE [2], this problem has been addressed by distinguishing between the different flow regimes and avoiding the hyperbolic ones. Subsequently, FINESSE has been used in combination with the a new MHD stability code PHOENIX to determine the stability of transsonic flows in the second elliptic flow regime for tokamak as well as accretion disks (Goedbloed et al. [17,16]). Hence, although the duo FINESSE–PHOENIX has been used for several cases and produced important physical results, the second part of it has not yet been documented in the literature. This is done here.

The magnetohydrodynamical (MHD) model is used to describe the macroscopic behaviour of the plasma. The tokamak or disk equilibrium is then modeled by a stationary solution of the ideal MHD equations taking the plasma flows into account. We will restrict our numerical analysis to stationary solutions which are either translationally symmetric or axisymmetric, consisting of nested closed flux surfaces contained within an arbitrarily shaped outer boundary. The stationary states are all computed with FINESSE [2] in the elliptic flow regime, where a split between equilibrium and perturbations can meaningfully be performed. The perturbations about this equilibrium are solved by means of the linearized MHD equations, which may include dissipative effects. The stability analysis itself is done in a flux coordinate system based on the specific equilibrium to obtain reliable and accurate results, as in e.g. CASTOR [37] and ERATO [25].

PHOENIX, in its original algorithmic design based on the widely used and rigorously tested CASTOR code [37], is able to perform a stability analysis of any 2D elliptic equilibrium with or without flow. The flow itself may be purely toroidal or both toroidal and poloidal. In the latter case, the poloidal rotation is not introduced in the first place with application to tokamaks as a goal, but rather to treat the enormous range of astrophysical plasmas, e.g. in accretion disks, that have large flows in the poloidal plane. For those plasmas, a fluid model is quite appropriate. For tokamaks, the fluid model may not always be adequate, as indicated by Stix [50], Hirshman [30], Shaing and Hirshman [47], Taguchi [53], Hsu et al. [33] and Morris et al. [38]. These authors discussed that in a tokamak the poloidal flow is damped due to viscous drag. This drag will not be taken into account. Nevertheless, the fluid solutions could be useful to guide simulations with particle-in-cell methods.

PHOENIX makes use of a finite element representation of the dynamics across flux surfaces in combination with a Galerkin method, which provides a flexible and highly accurate numerical approximation. The Galerkin has been exploited because it is more generally applicable, in particular to dissipative plasmas. This method has been widely used in spectral studies for dissipative plasmas (e.g. ERATO [25] and CASTOR [37]), based on concepts discussed by Strang and Fix [51]. Convergence for spectra has been a central issue in these studies, starting with the book by Gruber and Rappaz [24], but later extended to dissipative plasmas in many paper by Kerner et al. (see in particular the paper about CASTOR [37]). Note that the Galerkin

method has been chosen in particular because it is so much more powerful than the ideal MHD variational principle. Recently, a new code CASTOR–FLOW [52], also based on the CASTOR code [37], has been presented. This code is also able to take into account the plasma flow, but only in the toroidal direction and it is not generalized to gravitating plasmas of interest for astrophysical studies.

In general, stability studies in linear dissipative MHD give rise to non-Hermitian matrices and complex generalized eigenvalue problems. Ideal MHD spectral analysis of flowing equilibria also yield complex eigenvalues. Therefore, the discretization used, as well as the linear eigenvalue solver, has to be chosen carefully to avoid non-physical eigenvalues. The computation of the eigenvalues and eigenfunctions has been done by making use of the Jacobi–Davidson algorithm [48]. This recently developed powerful algorithm is an iterative Krylov subspace method, and we demonstrate its use for MHD spectroscopy in this paper.

The paper is organized as follows. In Section 2, we present the basic equations, discuss the equilibrium considerations, the spectral equations, the straight field line coordinates, and the projections used. In Section 3, the spectral analysis is presented. This section is split into three sections where the quadratic forms, the employed discretization, and the Jacobi–Davidson algorithm [48] are presented in full detail. In Section 4, new results are presented along with a reproduction of some standard static MHD spectral results. The new results provide many new test cases, covering cases with purely toroidal flow, with or without gravity, and cases with both toroidal and poloidal flow, again with or without gravity. Finally, in Section 5 we summarize and present our conclusions. Appendix A contains the equations which describe equilibria with purely toroidal flow, with or without gravity. For completeness and further reference, the matrix elements as they appear in the actual implementation are listed in Appendix B.

2. Basic equations

The plasma inside a tokamak or accretion disk can in a first, macroscopic approximation be modeled by making use of the single-fluid MHD equations. These equations are:

$$\frac{\partial \rho}{\partial t} = -\nabla \cdot (\rho \mathbf{v}), \tag{1}$$

$$\rho \frac{\partial \mathbf{v}}{\partial t} = -\rho \mathbf{v} \cdot \nabla \mathbf{v} - \nabla p + \mathbf{j} \times \mathbf{B} - \rho \nabla \Phi_{\text{grav}}, \tag{2}$$

$$\frac{\partial p}{\partial t} = -\mathbf{v} \cdot \nabla p - \gamma p \nabla \cdot \mathbf{v}, \tag{3}$$

$$\frac{\partial \mathbf{B}}{\partial t} = -\nabla \times \mathbf{E}, \tag{4}$$

where the variables ρ, $\mathbf{v}$, p, $\mathbf{B}$, Φ_{grav} and γ are the density, velocity, thermal pressure, magnetic field, external gravitational potential and the ratio of the specific heats, respectively. Here, the current density $\mathbf{j} = \nabla \times \mathbf{B}$. Furthermore, the simplified Ohm's law $\mathbf{E} = -\mathbf{v} \times \mathbf{B} + \eta \mathbf{j}$ and the equation $\nabla \cdot \mathbf{B} = 0$ must be satisfied. Here, η is the resistivity. The relation between the thermal pressure p and plasma temperature T is expressed by the ideal gas law, $p = \rho T$. We have used a dimensionalization such that the permeability of vacuum $\mu_0 = 1$. Notice that in the equation for the internal energy we neglect the non-ideal term $(\gamma - 1)\eta \mathbf{j}^2$. This assumption has also been used in the CASTOR code [37].

2.1. Equilibrium considerations

It is assumed that equilibria with toroidal and poloidal flow inside a tokamak or accretion disk are time-independent and that the resistivity can be neglected for the characterization of the equilibrium topology. Such equilibria have to satisfy the coupled generalized Grad–Shafranov equation and algebraic Bernoulli equation for the squared poloidal Alfvén Mach number $M^2 \equiv \rho v_{\text{p}}^2 / B_{\text{p}}^2$, where v_{p} and B_{p} are the poloidal velocity and poloidal magnetic field, respectively [29,17]. The equilibrium quantities can then be written as

$$
\begin{aligned}
&p = \rho^{\gamma} S, \\
&\mathbf{B} = \nabla\varphi \times \nabla\Psi + B_{\varphi}\mathbf{e}_{\varphi}, \quad RB_{\varphi} = \frac{I + \chi'\Omega R^2}{1 - M^2}, \\
&\mathbf{V} = \frac{\chi'}{\rho}\nabla\varphi \times \nabla\Psi + V_{\varphi}\mathbf{e}_{\varphi}, \quad \frac{V_{\varphi}}{R} = \frac{\Omega + (\chi'/\rho)I/R^2}{1 - M^2},
\end{aligned}
\tag{5}
$$

where the entropy S, the poloidal velocity stream function χ, poloidal vorticity–current density stream function I and the derivative of the electric potential Ω are arbitrary functions which only depend on the poloidal magnetic flux function $\Psi(R, Z)$. Here, R is the radius, Z is the vertical coordinate, φ is the toroidal angle in an (R, Z, φ) coordinate system and the prime indicates the derivative with respect to Ψ. Codes which are able to compute the numerical solution of the generalized Grad–Shafranov and Bernoulli equation are CLIO [45], FINESSE [2] and FLOW [26]. FINESSE takes special care of the existence of elliptic and hyperbolic flow regimes (Zelazny et al. [55]), which ensures that the solution always lies in one of the three existing elliptic flow regimes, namely sub-slow, slow, and fast flow regime. CLIO and FINESSE are both finite element codes and use a Picard iteration scheme while FLOW uses a multi-grid approach to solve the coupled generalized Grad–Shafranov and Bernoulli equation. Besides the numerical approach, the codes also differ in taking into account different physical effects. The FINESSE code is able to take into account external gravity. Meanwhile, FLOW is able to handle finite pressure anisotropy. The static or stationary equilibria used in this paper are computed using the FINESSE code. This code uses an isoparametric bicubic Hermite finite element method in combination with an (inner) Picard iteration and an extra outer iteration combined with an algebraic solver for the Bernoulli equation in case of poloidally flowing equilibria to compute the solution. The imposed boundary conditions are such that the boundary represents the last closed flux surface. The geometry of a tokamak or accretion disk for a circular cross-section is illustrated in Fig. 1. For the computations, the major radius of the geometric axis R_0 and the radius a of the last closed flux surface enter through the inverse aspect ratio $\epsilon \equiv a/R_0$. The FINESSE code recovers the solution for static equilibria as produced by HELENA [34] and extends the latter to handle equilibria with purely toroidal flow with or without gravity. The complete details of this extension for the various cases implemented can be found in Appendix A.

2.2. Spectral equations

The MHD equations (1)–(4) are linearized about the *time-independent* equilibrium with *time-dependent* fluctuations,

$$
y(\mathbf{r}, t) = y_0(\mathbf{r}) + y_1(\mathbf{r})\mathrm{e}^{\lambda t} \tag{6}
$$

where from now on we suppress the subscript 0. The linearized resistive MHD equations are

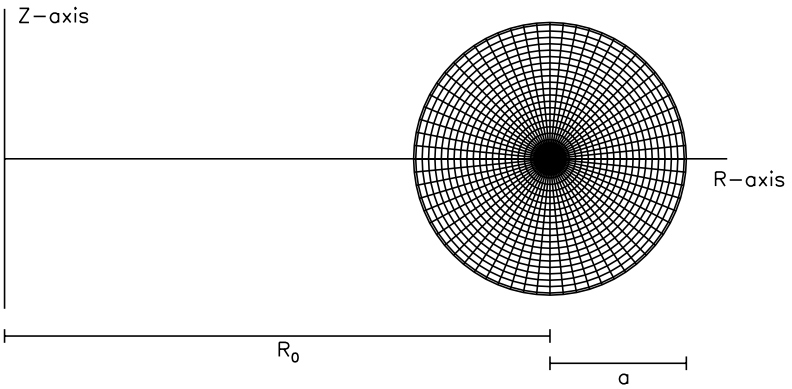

Fig. 1. The geometry of a tokamak or accretion disk plasma with a circular poloidal cross-section. Here, R_0 is the major radius of the geometric axis and a is the radius of the last closed flux surface.

$$\lambda\rho_1 = -\nabla\cdot(\rho\mathbf{v}_1) - \nabla\cdot(\rho_1\mathbf{V}), \tag{7}$$

$$\lambda\rho\mathbf{v}_1 = -\rho_1\mathbf{V}\cdot\nabla\mathbf{V} - \rho(\mathbf{v}_1\cdot\nabla\mathbf{V} + \mathbf{V}\cdot\nabla\mathbf{v}_1) - \nabla(\rho T_1 + \rho_1 T) + (\nabla\times\mathbf{B})\times(\nabla\times\mathbf{A}_1) - \mathbf{B}\times(\nabla\times\nabla\times\mathbf{A}_1) - \rho_1\nabla\Phi_{\text{grav}}, \tag{8}$$

$$\lambda\rho T_1 = -\rho_1\mathbf{V}\cdot\nabla T - \rho\mathbf{v}_1\cdot\nabla T - \rho\mathbf{V}\cdot\nabla T_1 - (\gamma-1)(\rho T_1 + \rho_1 T)\nabla\cdot\mathbf{V} - (\gamma-1)p\nabla\cdot\mathbf{v}_1, \tag{9}$$

$$\lambda\mathbf{A}_1 = \mathbf{v}_1\times\mathbf{B} + \mathbf{V}\times(\nabla\times\mathbf{A}_1) - \eta\nabla\times(\nabla\times\mathbf{A}_1), \tag{10}$$

where $\mathbf{A}_1$ is the perturbed vector potential. The perturbed vector potential formulation is used to make sure that the perturbed magnetic field $\mathbf{B}_1 = \nabla\times\mathbf{A}_1$ always satisfies the equation $\nabla\cdot\mathbf{B}_1 = 0$.

2.3. Straight field line coordinates

The linearized resistive MHD equations (7)–(10) are expressed in straight field coordinates. In these coordinates the magnetic field lines become straight in the (ϑ,φ)-plane, where ϑ is the straight field line angle. The contravariant and covariant base vectors of this non-orthogonal coordinate system are

$$\begin{aligned}
&\mathbf{a}^1 = \nabla s, \quad \mathbf{a}_1 = fJ\nabla\vartheta\times\nabla\varphi,\\
&\mathbf{a}^2 = \nabla\vartheta, \quad \mathbf{a}_2 = fJ\nabla\varphi\times\nabla s,\\
&\mathbf{a}^3 = \nabla\varphi, \quad \mathbf{a}_3 = fJ\nabla s\times\nabla\vartheta,
\end{aligned} \tag{11}$$

where $s \equiv \sqrt{\Psi}$, where Ψ is now a normalized flux function reaching unit value at the boundary, $f = \mathrm{d}\Psi/\mathrm{d}s$, and the Jacobian J is defined by

$$J = (\nabla\Psi\times\nabla\vartheta\cdot\nabla\varphi)^{-1}. \tag{12}$$

Knowing the base vectors, it is straightforward to derive the components of the metric tensor g_{ij}. The non-zero elements are

$$\begin{aligned}
&g^{11} = |\nabla s|^2, \quad g_{11} = \frac{f^2J^2}{R^2}|\nabla\vartheta|^2,\\
&g^{12} = \nabla s\cdot\nabla\vartheta = g^{21}, \quad g_{12} = -\frac{fJ^2}{R^2}\nabla\Psi\cdot\nabla\vartheta = g_{21},\\
&g^{22} = |\nabla\vartheta|^2, \quad g_{22} = \frac{J^2}{R^2}|\nabla\Psi|^2,\\
&g^{33} = |\nabla\varphi|^2 = \frac{1}{R^2}, \quad g_{33} = R^2.
\end{aligned} \tag{13}$$

These are needed to express the linearized resistive MHD equations in straight field line coordinates. Furthermore, in these coordinates one can derive an expression for the safety factor q,

$$\left.\frac{\mathrm{d}\varphi}{\mathrm{d}\vartheta}\right|_{\text{field line}} = \frac{\mathbf{B}\cdot\nabla\varphi}{\mathbf{B}\cdot\nabla\vartheta} = \frac{B_\varphi J}{R} = q(\Psi). \tag{14}$$

Using this expression and Eq. (5) for the toroidal magnetic field, the Jacobian J can be expressed as follows:

$$J = qR^2\frac{1-M^2}{I+\chi'\Omega R^2}. \tag{15}$$

Note the considerably more complex relation between J and q than for static equilibria or equilibria with purely toroidal flow.

2.4. Projections

The equation for the perturbed velocity $\mathbf{v}_1$ (8) and perturbed vector potential $\mathbf{A}_1$ (10) are projected on the straight field line coordinates. This kind of projection is similar as the one used in ERATO [25] and CASTOR [37]. The perturbed velocity has been projected as follows:

$$\mathbf{v}_1 \equiv \bar{v}_1 J \nabla\vartheta \times \nabla\varphi + \frac{1}{if}\bar{v}_2 J \nabla\varphi \times \nabla\Psi + \frac{1}{if}\bar{v}_3 J \mathbf{B}, \tag{16}$$

where $\bar{v}_1$ and $\bar{v}_2$ actually correspond to the contravariant velocity components, while $\bar{v}_3$ represents the slow magnetosonic modes in the case of a homogeneous equilibrium. Notice the subtle difference, J versus R^2 factor in front of the contravariant components, between (16) for $\mathbf{v}_1$ and the expression used in CASTOR [37]. This is due to the more complicated expression for the Jacobian J in the case of equilibria with both toroidal and poloidal flows.

In contrast with the perturbed velocity, the perturbed vector potential is expressed in terms of the covariant components:

$$\mathbf{A}_1 \equiv \frac{1}{if}\overline{A}_1 \nabla\Psi + \overline{A}_2 \nabla\vartheta + \overline{A}_3 \nabla\varphi. \tag{17}$$

Furthermore, the perturbed density and temperature have been rescaled as follows:

$$\bar{\rho} \equiv s\rho_1, \quad \overline{T} \equiv sT_1. \tag{18}$$

3. Spectral analysis

3.1. Quadratic form

Before applying the projections defined in the previous section, the linearized resistive MHD equations (7)–(10) are written in quadratic form

$$\lambda K^{(k)} = W^{(k)}, \tag{19}$$

where $k = 1, 2, 3,$ or 4 corresponds to the equation for the perturbed density ρ_1, velocity $\mathbf{v}_1$, temperature T_1, or vector potential $\mathbf{A}_1$, respectively. This quadratic form can be derived by multiplying the linearized equations by the appropriate perturbed quantity and then to integrate over the plasma volume V.

The equation of the perturbed density (7) has been multiplied with the complex conjugate of the perturbed density ρ_1^*. In this way the quadratic forms $W^{(1)}$ and $K^{(1)}$ are

$$W^{(1)} = \int\int\int \rho_1^*[-\nabla\cdot(\rho\mathbf{v}_1) - \nabla\cdot(\rho_1\mathbf{V})]\mathrm{d}V, \tag{20}$$

$$K^{(1)} = \int\int\int \rho_1^*\rho_1\,\mathrm{d}V. \tag{21}$$

For the equation of the perturbed velocity $\mathbf{v}_1$, temperature T_1 and vector potential $\mathbf{A}_1$ the same strategy has been used, multiplying with the complex conjugate of the perturbed velocity $\mathbf{v}_1^*$, temperature T_1^*, and vector potential $\mathbf{A}_1^*$, respectively. For the perturbed velocity the quadratic form $W^{(2)}$ reads

$$W^{(2)} = \int\int\int \mathbf{v}_1^*\cdot[-\nabla\Pi_1 + \mathbf{H} - \rho\mathbf{F} - \rho_1(\mathbf{C} + \nabla\Phi_{\mathrm{grav}})]\mathrm{d}V \tag{22}$$

$$= \int\int\int \Pi_1\nabla\cdot\mathbf{v}_1^*\,\mathrm{d}V + \int\int\int \mathbf{v}_1^*\cdot\mathbf{H}\,\mathrm{d}V - \int\int\int \rho\mathbf{v}_1^*\cdot\mathbf{F}\,\mathrm{d}V$$
$$- \int\int\int \rho_1\mathbf{v}_1^*\cdot(\mathbf{C} + \nabla\Phi_{\mathrm{grav}})\mathrm{d}V - \int\int\int \mathbf{n}\cdot\mathbf{v}_1^*\Pi_1\,\mathrm{d}S, \tag{23}$$

where

$$\Pi_1 = p_1 + \mathbf{B}\cdot\mathbf{B}_1, \tag{24}$$

$$\mathbf{H} = \mathbf{B}\cdot\nabla\mathbf{B}_1 + \mathbf{B}_1\cdot\nabla\mathbf{B}, \tag{25}$$

$$\mathbf{F} = \mathbf{V}\cdot\nabla\mathbf{v}_1 + \mathbf{v}_1\cdot\nabla\mathbf{V}, \tag{26}$$

$$\mathbf{C} = \mathbf{V}\cdot\nabla\mathbf{V}, \tag{27}$$

and $\mathbf{n}$ is the normal to the surface S which encloses the plasma volume V. Furthermore, notice that Π_1 and $\mathbf{H}$ are the perturbed total pressure and the linearized magnetic tension, respectively. The terms $\mathbf{F}$ and $\mathbf{C}$ combine linearized flow effects and the centrifugal effects from the equilibrium. The quadratic form $K^{(2)}$ is

$$K^{(2)} = \int\int\int \rho \mathbf{v}_1^* \cdot \mathbf{v}_1 \,\mathrm{d}V. \tag{28}$$

For the perturbed temperature, the quadratic forms $W^{(3)}$ and $K^{(3)}$ are

$$\begin{aligned} W^{(3)} = &- \int\int\int T_1^*(\rho_1 \mathbf{V}\cdot\nabla T + \rho \mathbf{v}_1 \cdot \nabla T + \rho \mathbf{V}\cdot\nabla T_1)\mathrm{d}V \\ &- (\gamma-1)\int\int\int T_1^*[(\rho T_1 + \rho_1 T)\nabla\cdot\mathbf{V} + p\nabla\cdot\mathbf{v}_1]\mathrm{d}V, \end{aligned} \tag{29}$$

$$K^{(3)} = \int\int\int \rho T_1^* T_1 \,\mathrm{d}V, \tag{30}$$

and for the perturbed vector potential the forms are

$$W^{(4)} = \int\int\int \mathbf{A}_1^* \cdot [-\mathbf{B}\times\mathbf{v}_1 + \mathbf{V}\times(\nabla\times\mathbf{A}_1) - \eta\nabla\times\nabla\times\mathbf{A}_1]\mathrm{d}V \tag{31}$$

$$\begin{aligned} &= -\int\int\int \mathbf{A}_1^*\cdot\mathbf{B}\times\mathbf{v}_1\,\mathrm{d}V + \int\int\int \mathbf{A}_1^*\cdot\mathbf{V}\times(\nabla\times\mathbf{A}_1)\mathrm{d}V \\ &\quad - \int\int\int \eta(\nabla\times\mathbf{A}_1^*)\cdot(\nabla\times\mathbf{A}_1)\mathrm{d}V + \oiint \eta\mathbf{A}_1^*\times(\nabla\times\mathbf{A}_1)\cdot\mathbf{n}\,\mathrm{d}S, \end{aligned} \tag{32}$$

$$K^{(4)} = \int\int\int \mathbf{A}_1^*\cdot\mathbf{A}_1\,\mathrm{d}V. \tag{33}$$

The currently implemented boundary conditions are the ones of a perfect conducting wall. For these conditions, the normal velocity component, the normal magnetic field component and the tangential electric field vanish at the wall. This leads to the boundary conditions

$$\bar{v}_1|_{\text{wall}} = 0, \quad \overline{A}_2|_{\text{wall}} = 0, \quad \overline{A}_3|_{\text{wall}} = 0. \tag{34}$$

For astrophysical applications these boundary conditions are strictly speaking inappropriate. However, these conditions have hardly any influence on sufficiently localized modes or global modes which are not significantly affected by the position of the wall. Regularity of the solutions on the magnetic axis implies

$$\bar{v}_1|_{\text{axis}} = 0, \quad \overline{A}_2|_{\text{axis}} = 0, \quad \overline{A}_3|_{\text{axis}} = 0. \tag{35}$$

3.2. Discretization

The discretization we employ in combination with the previously defined projections as follows. In the poloidal direction, the equations are discretized by making use of a spectral method. This means that every perturbed quantity is written as a finite sum of Fourier components:

$$f_1(\Psi,\vartheta,\varphi) = \sum_m \hat{f}_{1,m}(\Psi)\exp[\mathrm{i}(m\vartheta + n\varphi)], \tag{36}$$

where m and n are the poloidal and toroidal mode numbers, respectively. In the toroidal direction there is only need for one mode number due to the axisymmetry. In contrast, in the poloidal direction one needs more than one mode number because of mode coupling due to non-circular cross-section, gravitational stratification, and the toroidal geometry of the tokamak or accretion disk.

The normal Ψ dependence of the perturbed quantity $\hat{f}_{1,m}(\Psi)$ is discretized using a finite element method (FEM). The components $\bar{v}_1$, $\overline{A}_2$ and $\overline{A}_3$ are expanded in cubic Hermite elements, while quadratic elements are used to represent $\bar{v}_2$, $\bar{v}_3$ and $\overline{A}_1$. For the perturbed quantities $\bar{\rho}$ and $\overline{T}$ also quadratic elements are used. There are two basis functions per grid point used in the Ψ-direction for both the cubic and quadratic elements.

Using this mixed cubic and quadratic elements discretization prevents the creation of spurious eigenvalues [43]. This choice of elements for the perturbed vector potential ensures that the divergence of the perturbed magnetic field is numerically zero up to machine precision. In the quadratic forms mentioned above, we subsequently replace the complex conjugate of the perturbed quantities with every finite element used in its FEM expansion. This then corresponds to the standard Galerkin method in its weak form.

Applying this procedure leads to a generalized eigenvalue problem,

$$\mathbf{A}\mathbf{x} = \lambda \mathbf{B}\mathbf{x}, \tag{37}$$

where $\mathbf{x}$ denotes the vector of the expansion coefficients of the state vector $[\bar{\rho}, \bar{v}_1, \bar{v}_2, \bar{v}_3, \overline{T}, \overline{A}_1, \overline{A}_2, \overline{A}_3]^{\mathrm{T}}$, and matrices $\mathbf{A}$ and $\mathbf{B}$ correspond to the quadratic forms $W^{(k)}$ and $K^{(k)}$, respectively. The matrix elements of $\mathbf{A}$ and $\mathbf{B}$ can be found in the appendix. The number of expansion coefficients $N = 16 \times N_s \times N_m$, where N_s and N_m are the number of mesh points along the "radial" s-coordinate and the number of poloidal Fourier harmonics ($\sim \mathrm{e}^{\mathrm{i}m\vartheta}$), respectively. The matrix $\mathbf{B}$ is self-adjoint and positive definite, but $\mathbf{A}$ is always non-Hermitian even without flow and resistivity ($\eta = 0$). The matrices $\mathbf{A}$ and $\mathbf{B}$ have both block-tridiagonal structure, as shown in Fig. 2. This structure is due to the fact that every element extends over two radial intervals. Each sub-block of matrix $\mathbf{A}$ has the structure as indicated in Fig. 2, where the i, j's indicate the matrix elements of $\mathbf{A}$ for a given range of poloidal mode numbers m and m'. The matrix $\mathbf{B}$ has a similar sub-block structure and its matrix elements can also be found in Appendix B. All elements are listed in Appendix B. A similar matrix

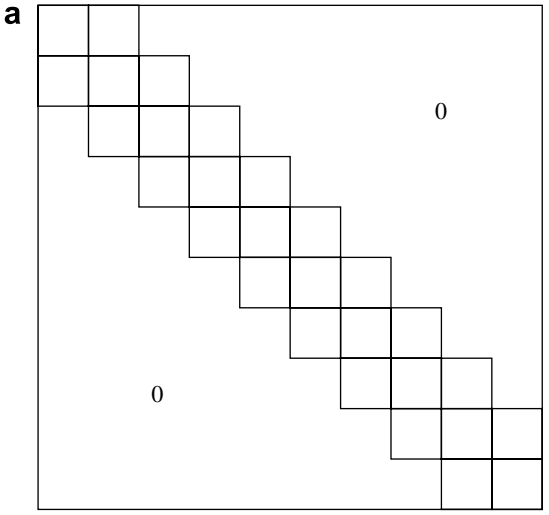

b

1,1	1,2	1,3	1,4				
2,1	2,2	2,3	2,4	2,5	2,6	2,7	2,8
3,1	3,2	3,3	3,4	3,5	3,6	3,7	3,8
4,1	4,2	4,3	4,4	4,5	4,6	4,7	4,8
5,1	5,2	5,3	5,4	5,5			
	6,2	6,3			6,6	6,7	6,8
	7,2	7,3			7,6	7,7	7,8
	8,2				8,6	8,7	8,8

Fig. 2. (a) The block-tridiagonal structure of matrix $\mathbf{A}$ and $\mathbf{B}$ with dimension $N = 16 \times N_s \times N_m$. (b) The structure of each sub-block of matrix $\mathbf{A}$.

structure has been used in the CASTOR code [37]. Due to the non-Hermitian property of $\mathbf{A}$ one needs an algorithm that can accurately solve the generalized eigenvalue problem (37). The two well known direct algorithms, QR (QZ) and inverse vector iteration [37], could have been used, but instead PHOENIX solves the generalized eigenvalue problem (37) by making use of the much more powerful iterative Jacobi–Davidson algorithm [48]. This algorithm will be discussed in the next section.

Before continuing the discussion how the PHOENIX code can also compute the ideal continuous MHD spectrum, we first briefly introduce the MHD continua themselves. The threefold ideal MHD spectrum consists of fast, Alfvén and slow subspectra, and is organized about the continuous parts, i.e. the slow and Alfvén continua, and a fast accumulation point at infinity. In the cylindrical limit (relevant for large aspect ratio and circular cross-section), the ideal MHD equation can be reduced to one ordinary second order differential equation in the radial coordinate r. This equation has been introduced by Hain and Lüst [27] and generalized for arbitary γ by Goedbloed [12] for a static equilibrium. Hameiri [28] and Bondeson et al. [3] extended the cylindrical case to plasmas with flow but without gravity. Recently, Keppens et al. [36] have included gravity. The inclusion of flow gives rise to a sixfold organization about Doppler shifted MHD continua, viz. Doppler shifted Alfvén continua $\Omega_{\mathrm{A}}^{\pm}$ and Doppler shifted slow continua $\Omega_{\mathrm{S}}^{\pm}$,

$$\Omega_{\mathrm{A}}^{\pm} = \mathbf{k}\cdot\mathbf{V} \pm \omega_{\mathrm{A}} = n\Omega + (M \pm 1)\omega_{\mathrm{A}}, \tag{38}$$

$$\Omega_{\mathrm{S}}^{\pm} = \mathbf{k}\cdot\mathbf{V} \pm \omega_{\mathrm{S}} = n\Omega + (M \pm M_{\mathrm{c}})\omega_{\mathrm{A}}, \tag{39}$$

together with fast accumulation points at $\pm\infty$ where the modes have a single $\exp[\mathrm{i}(m\vartheta + n\varphi)]$ dependence in the cylindrical limit (Goedbloed et al. [17]). Here, ω_{A} and ω_{S} are the Alfvén frequency and slow frequency. Furthermore, the cusp $M_{\mathrm{c}} = \sqrt{\gamma p/(\gamma p + B^2)}$ is the ratio of the sound speed over the magnetosonic speed. Moreover, an additional Eulerian entropy continuum is given by

$$\Omega_{\mathrm{E}} = \mathbf{k}\cdot\mathbf{V} = n\Omega + M\omega_{\mathrm{A}}, \tag{40}$$

which does not couple to the remainder of the spectrum, as shown by Goedbloed et al. [18]. This entropy continuum will show up in any Eulerian computational approach for computing ideal MHD continua.

For the computation of the continuous MHD spectra, a method described by Poedts et al. [42] has been used. This method, in essence, replaces on each individual flux surface the Hermite elements by $\log(\epsilon)$ and the quadratic elements by $1/\epsilon$, with small ϵ. In this way the perturbed quantities approximate the singular behaviour of the continuous spectrum as described by Pao [40] and Goedbloed [13] for a static, axisymmetric, and toroidal plasma. Recently, Goedbloed et al. [17] have extended this work to plasmas with toroidal and poloidal flows and gravity. In this procedure, one instead of two basis functions per grid point is sufficient. One then obtains a small generalized eigenvalue problem per flux surface of order $8N_m$. The resulting eigenvalue problem is solved using a QR method and a scan over all flux surfaces yields detailed information on all MHD continua.

3.3. Jacobi–Davidson algorithm

The Jacobi–Davidson (JD) algorithm [48] has been used to compute the eigenvalues of our large generalized eigenvalue problem. For completeness, we present the basic steps involved in the JD algorithm, following the description presented by Nool and van der Ploeg [39]. The generalized eigenvalue problem of the linearized MHD equations (37) can be written as a standard eigenvalue problem

$$\mathbf{Q}\mathbf{x} = \mu\mathbf{x}, \tag{41}$$

where $\mathbf{Q} = (\mathbf{A} - \sigma\mathbf{B})^{-1}\mathbf{B}$ and we introduced an inverse shifted eigenvalue $\mu = 1/(\lambda - \sigma)$. Here, σ is a specified target frequency in whose neighborhood we wish to compute a number of eigenvalues and eigenvectors at once.

In the JD algorithm the eigenvector $\mathbf{x}$ is approximated by a linear combination of k-search vector $\mathbf{v}_j$ with $j = 1, 2, \ldots, k$, where k is very small compared to the number of expansion coefficients N. Using the modified Gram–Schmidt method [21], the vectors $\mathbf{v}_j$ are made orthonormal to each other. The search directions $\mathbf{v}_j$ are used as columns for the $N \times k$ matrix $\mathbf{V}_k$. Using this matrix the eigenvector $\mathbf{x}$ can be approximated by $\mathbf{V}_k\mathbf{s}$ for

some k-vector $\mathbf{s}$. Notice that the matrix $\mathbf{V}_k$ satisfies the following property: $\mathbf{V}_k^*\mathbf{V}_k = \mathbf{I}_k$, where $\mathbf{I}_k$ is the unit $k \times k$ matrix. Here, the star indicates the conjugate transpose.

Replace in the standard eigenvalue equation (41) the eigenvector $\mathbf{x}$ and the eigenvalue μ by its approximation $\mathbf{V}_k\mathbf{s}$ and θ, respectively. In this way the residual vector $\mathbf{r} = \mathbf{Q}\mathbf{V}_k\mathbf{s} - \theta\mathbf{V}_k\mathbf{s}$, which is orthogonal to the k search vectors. The standard eigenvalue problem for the eigenvalue θ becomes

$$\mathbf{V}_k^*\mathbf{Q}\mathbf{V}_k\mathbf{s} = \theta\mathbf{s}. \tag{42}$$

The order of the matrix $\mathbf{V}_k^*\mathbf{Q}\mathbf{V}_k$ is k, which is small. In fact it can be so small, that this problem can be solved directly by, for example, a QR method. The eigenvalue of this problem with the largest modulus is then used to approximate the eigenvalue μ. Notice that the vector $\mathbf{s}$ is its associated eigenvector.

The following procedure is used to obtain a new search direction. Let the normalized vector $\mathbf{u} = \mathbf{V}_k\mathbf{s}$ be the approximation of the eigenvector $\mathbf{x}$ of the standard eigenvalue problem (41). Then the eigenvalue μ can be approximated by $\theta = \mathbf{u}^*\mathbf{Q}\mathbf{u}$. We define the matrix $\mathbf{P} \equiv \mathbf{u}\mathbf{u}^*$, which is the orthogonal projector onto the subspace spanned by $\{\mathbf{u}\}$. Its complementary projector $\mathbf{I}_N - \mathbf{P}$ projects a vector on a subspace perpendicular to the subspace spanned by $\{\mathbf{u}\}$. This subspace is denoted by $\mathbf{u}^\perp$. Any vector $\mathbf{x} \in \mathbb{C}^N$ can be written as $\mathbf{x} = \mathbf{x}_1 + \mathbf{x}_2$, with $\mathbf{x}_1 \in \text{span}\{\mathbf{u}\}$ and $\mathbf{x}_2 \in \mathbf{u}^\perp$. In this case, the eigenvector $\mathbf{x}$ can be written as $\mathbf{x} = \mathbf{u} + \mathbf{z}$, where the correction vector $\mathbf{z} \perp \mathbf{u}$. The matrix $\mathbf{Q}$ can be restricted to $\mathbf{u}^\perp$ as follows:

$$\mathbf{Q}_\mathbf{P} = (\mathbf{I}_N - \mathbf{P})\mathbf{Q}(\mathbf{I}_N - \mathbf{P}). \tag{43}$$

Jacobi–Davidson method for $\mathbf{Q}\mathbf{x} = \mu\mathbf{x}$

Parameters: $it_{\max}$, tol_{JD}, it_{SOL}, tol_{SOL}

step 0: initialize
Choose a non–trivial initial vector $\mathbf{v}_1$ with $|\mathbf{v}_1| = 1$;
set $\mathbf{V}_1 = [\mathbf{v}_1]$; $\mathbf{W}_1 = [\mathbf{Q}\mathbf{v}_1]$; $it = 1$

step 1: update the projected system
Compute the last row and column of $\mathbf{H}_k := \mathbf{V}_k^*\mathbf{W}_k$

step 2: solve and choose the approximate eigensolution of projected system
Compute the eigenvalues $\theta_1, \ldots, \theta_k$ of $\mathbf{H}_k$ and
choose $\theta := \theta_j$ with $|\theta_j|$ maximal and $\theta_j \neq \mu_i$ for $i = 1, \ldots, n_{\text{ev}}$;
compute the associated eigenvector $\mathbf{s}$ with $|\mathbf{s}| = 1$

step 3: compute Ritz vector and check accuracy
Let $\mathbf{u}$ be the Ritz vector $\mathbf{V}_k\mathbf{s}$; compute the vector $\mathbf{r} := \mathbf{W}_k\mathbf{s} - \theta\mathbf{u}$;
`if` the residual $\hat{\mathbf{r}} := (\mathbf{A} - (\sigma + \frac{1}{\theta})\mathbf{B})\mathbf{u}$ satisfies $|\hat{\mathbf{r}}|/(|\sigma + \frac{1}{\theta}|) < tol_{\text{JD}}$ `then`
$n_{\text{ev}} := n_{\text{ev}} + 1$; $\mu_{n_{\text{ev}}} = \theta$
`else if` $it == it_{\max}$ `stop`
`end if`

step 4: solve correction equation approximately with it_{SOL} steps of GMRES (with tolerance tol_{SOL})
Determine an approximate solution $\tilde{\mathbf{z}}$ of $\mathbf{z}$ in
$(\mathbf{I} - \mathbf{P})(\mathbf{Q} - \theta\mathbf{I})(\mathbf{I} - \mathbf{P})\mathbf{z} = -\mathbf{r} \quad \wedge \quad \mathbf{u}^*\mathbf{z} = 0$

step 5: add new search direction
$k := k + 1$; $it := it + 1$; call MGS$[\mathbf{V}_{k-1}, \tilde{\mathbf{z}}]$; set $\mathbf{V}_k = [\mathbf{V}_{k-1}, \tilde{\mathbf{z}}]$;
$\mathbf{W}_k = [\mathbf{W}_{k-1}, \mathbf{Q}\tilde{\mathbf{z}}]$;
`goto` **step 1**

Fig. 3. Jacobi–Davidson algorithm adopted from Nool and van der Ploeg [39]. Here, $\text{it}_{\max}$, tol_{JD}, tol_{SOL}, n_{ev} and MGS are the maximum number of iterations, tolerance of the JD algorithm, tolerance for solving the correction equation, number of found eigenvalues and the modified Gram–Schmidt method, respectively.

Rewrite this equation to find an expression for $\mathbf{Q}$ and substitute this expression into the standard eigenvalue problem (41) to obtain

$$(\mathbf{Q_P} - \mu \mathbf{I}_N)\mathbf{z} = -\mathbf{r} + (\mu - \theta - \mathbf{u}^*\mathbf{Q}\mathbf{z})\mathbf{u}, \tag{44}$$

where we used that $\mathbf{Q}\mathbf{u} - \theta\mathbf{u} = \mathbf{r}$ and $\mathbf{z} \perp \mathbf{u}$. From this equation we derive that the eigenvalue $\mu = \theta + \mathbf{u}^*\mathbf{Q}\mathbf{z}$ by making use of $\mathbf{r} \perp \mathbf{u}$. Since eigenvalue μ is unknown and its best approximation is θ, we have to replace μ by θ to obtain the correction equation for $\mathbf{z}$,

$$(\mathbf{I}_N - \mathbf{P})(\mathbf{Q} - \theta \mathbf{I}_N)(\mathbf{I}_N - \mathbf{P})\mathbf{z} = -\mathbf{r}, \tag{45}$$

with $\mathbf{u}^*\mathbf{z} = 0$. The correction equation (45) only needs to be solved approximately to obtain a sufficient accurate solution needed for the new search direction. An iterative method, like GMRES [44], could be used for this. The approximated solution of the correction vector $\mathbf{z}$ is made orthogonal to the previous search vector using the modified Gram–Schmidt method [21], and this yields the new search directions $\mathbf{v}_{k+1}$. Then k is increased by 1 and the procedure can be iterated. Our implementation of the JD method for the computations for several eigenvalues is shown in Fig. 3. The typical values for the maximum number of iterations of JD algorithm $\mathrm{it}_{\max} = 100$, tolerance of JD algorithm $\mathrm{tol}_{\mathrm{JD}} = 10^{-6}$, maximum number of iterations for solving the correction equation $\mathrm{it}_{\mathrm{SOL}} = 10$, and tolerance for solving the correction equation $\mathrm{tol}_{\mathrm{SOL}} = 10^{-4}$.

4. MHD spectral results for flowing plasmas

In the PHOENIX code the eigenvalues are normalized to the Alfvén time on the magnetic axis:

$$\hat{\lambda} = R_{\mathrm{M}}\lambda / v_{\mathrm{A}}, \tag{46}$$

where R_{M} and v_{A} are the major radius of the magnetic axis and the Alfvén speed on the magnetic axis, respectively.

4.1. Test cases for static and toroidally rotating Soloviev like equilibria: ideal unstable global modes

As a first test we compare the PHOENIX code with other existing codes, like CASTOR [37], ERATO [25], MARS [4], NOVA [9] and PEST-1 [23], by investigating an isolated unstable global mode. For this test case, we used the analytical solution of the Grad–Shafranov equation [22,46] given by Soloviev [49] for the equilibrium. For the cross-sections we consider two elliptical, $E = 2$, and one circular, $E = 1$, cross-section together with inverse aspect ratio $\epsilon = 1/3$. The PHOENIX results are presented in Table 1, together with the results of the other codes, as taken from Kerner et al. [37]. In Table 1, m, n, and $q(0)$ are the poloidal mode number, the toroidal mode number, and the safety factor at the magnetic axis, respectively. It is clear from this table that the agreement between the different codes is within 1%.

As far as we know, there is no simple published test case for an equilibrium with purely toroidal flow. Therefore, we start with an equilibrium based on the Soloviev solution of the first static test case. In case the plasma rotates, the temperature is assumed to be a flux function. For the equilibrium the following flux functions have been used:

$$\begin{aligned} &I^2(\Psi) = A, \quad \rho_0(\Psi) = 1, \\ &p_0(\Psi) = AB(1 - 0.9\Psi), \end{aligned} \tag{47}$$

Table 1
Comparison of the eigenvalue $\hat{\lambda}$ for a specific Soloviev equilibrium with an inverse aspect ratio $\epsilon = 1/3$ from different ideal MHD spectral codes

m	n	$q(0)$	E	PHOENIX	CASTOR	ERATO	MARS	NOVA	PEST-1
[−4, 6]	−2	0.3	2	1.255	1.255	1.26	1.26	1.256	1.252
[−3, 7]	−2	0.7	2	0.284	0.284	0.284	0.284	0.283	0.283
[−8, 14]	−3	0.75	1	0.05397	0.05384	0.0541	0.0533	–	–

The latter entries are adopted from Kerner et al. [37].

where A is a scale factor which has to be computed as part of the equilibrium solution and $B = 2.5$. More details about equilibria with purely toroidal flow can be found in Appendix A. The cross-section has been specified by ellipticity $E = 2$, triangularity $T = 0.2$, and rectangularity $Q = 0.01$ and the inverse aspect ratio $\epsilon = 0.381966$. The safety factor on the magnetic axis $q(0) = 0.7$. Fig. 4 shows the growth rate and oscillation frequency as function of the rotation frequency $\Omega(0)$ on the magnetic axis. Here, we used a toroidal mode

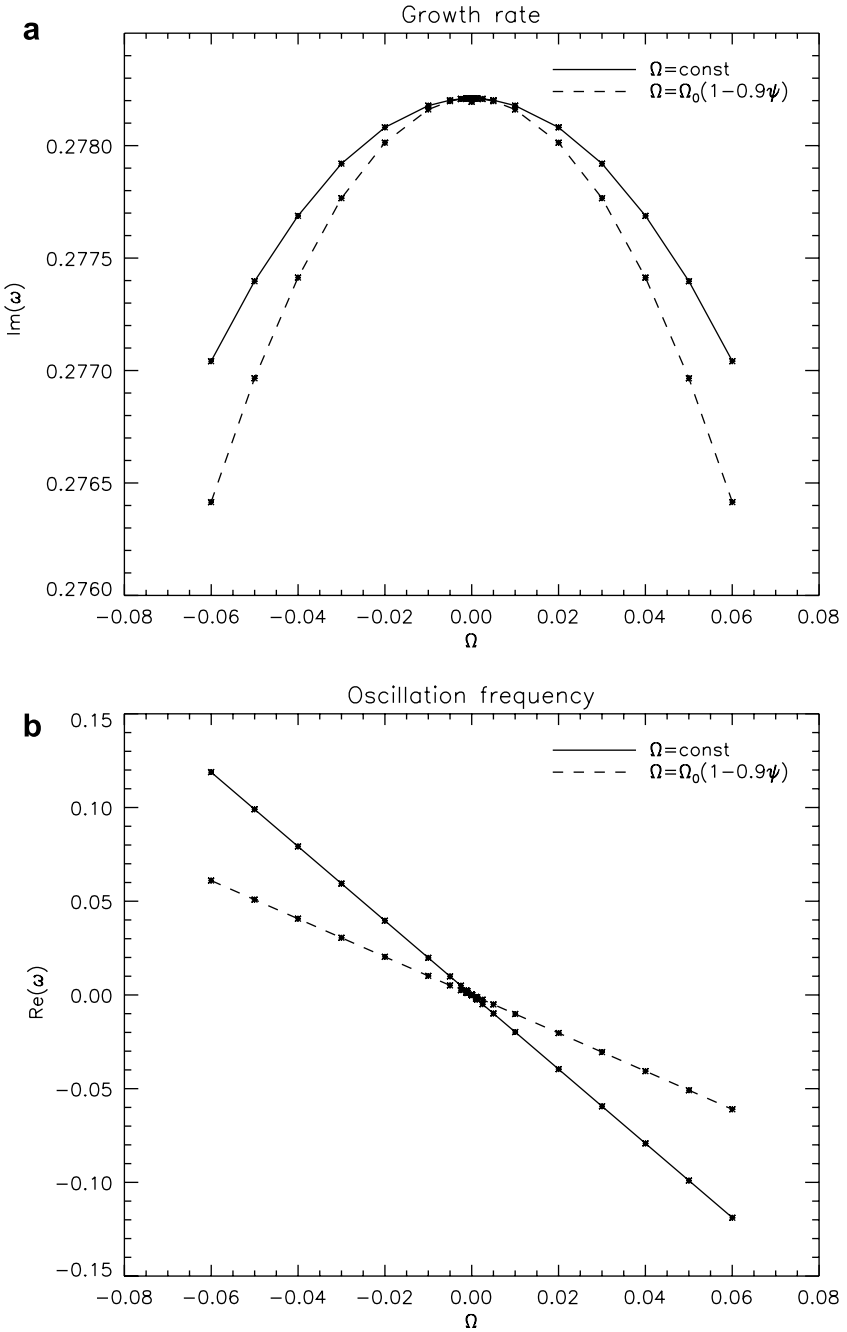

Fig. 4. The growth rate (a) and oscillation frequency (b) for rigidly rotating equilibrium (solid) versus an equilibrium with sheared toroidal flow (dashed). The rotation frequency Ω on the x-axis is the value on the magnetic axis and has been normalized with respect to the Alfvén time on the magnetic axis.

number $n = -2$ and poloidal mode numbers $m = [-3, 7]$. Computations are shown for both rigidly rotating, as well as sheared rotating profiles $\Omega(\Psi)$. It is clear from this figure that this particular unstable mode becomes less unstable if one includes toroidal flow, regardless of the direction of the flow. If the toroidal flow has some shear the mode becomes even more stable. This stabilizing effect has also been found by Chandra et al. [8] for classical and neoclassical tearing modes. The figure also shows that the oscillation frequency scales linearly with the rotation frequency on the magnetic axis ($\Omega = \text{const} \Rightarrow \text{Re}(\omega) \approx -1.98\Omega(0)$ and $\Omega = \Omega_0(1 - 0.9\Psi) \Rightarrow \text{Re}(\omega) \approx -1.02\Omega(0)$).

4.2. Resistive internal kink mode

A severe test for a MHD stability code is the computation of the internal kink mode. In this case, we compute the resistive internal kink mode. The equilibrium is specified by a circular cross-section, inverse aspect ratio $\epsilon = 0.1$ and the profiles

$$p = AB(1 - \Psi), \tag{48}$$

$$\langle j_\varphi \rangle = j_0(1 - \Psi), \tag{49}$$

where $\langle j_\varphi \rangle$ is the average toroidal current density. The parameters are chosen such that the safety factor on the magnetic axis $q(\Psi = 0) = 0.9$ and the average poloidal plasma beta $\beta_{\text{pol}} = 0.1$. The average poloidal plasma beta is defined as

$$\beta_{\text{p}} \equiv 2\frac{\int\int p\,\mathrm{d}S}{\left(\frac{1}{2\pi}\oint \mathbf{B}_{\text{p}} \cdot \mathrm{d}\mathbf{l}\right)^2}, \tag{50}$$

where S is the area of the poloidal cross-section and $\mathbf{l}$ is the contour which enclosed the area S. For the stability analysis we have used a toroidal mode number $n = -1$ and poloidal mode numbers $m = [-1, 3]$. To obtain an accurate solution, 1001 mesh points have been used in combination with mesh accumulation around the $q = 1$ and $q = 2$ surface. Fig. 5 shows the growth rate of the resistive internal kink mode against the resistivity. The resistive mode seen in the figure is the resistive interchange mode which scales as $\eta^{1/3}$. This numerical example shows that the PHOENIX code can accurately handle small values for resistivity, at least as small

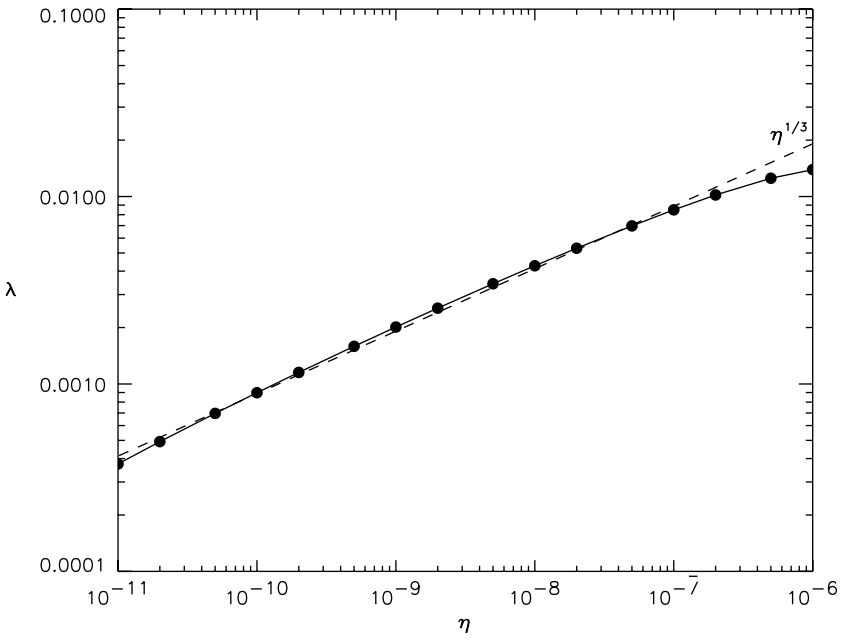

Fig. 5. The growth rate of the resistive internal kink mode for a equilibrium with a circular cross-section and inverse aspect ratio $\epsilon = 0.1$.

as 10^{-11}. A detailed study of resistive instabilities in a tokamak is given by, for example, Huysmans et al. [35] and Bondeson et al. [5].

4.3. Toroidal Flow induced Alfvén Eigenmode

Another stringent test is to find the stable, resonantly damped, global Toroidal Flow induced Alfvén Eigenmode (TFAE) which was found by van der Holst et al. [31]. They use an equilibrium where the density is assumed to be a flux function. We use the following flux functions for the equilibrium:

$$\begin{aligned} I^2(\Psi) &= A(1 - 0.0285\Psi + 0.01045\Psi^3), \quad \rho(\Psi) = 1 - 0.85\Psi, \\ p_0(\Psi) &= AB(1 - 1.1\Psi + 0.2\Psi^2), \quad \Omega(\Psi) = C, \end{aligned} \tag{51}$$

where $A = 87$, $B = 0.0217$ and $C = 0.0952$. These flux functions differ slightly from the ones used by van der Holst et al. [31]. Using the same strategy as described in that article we were able to find the TFAE, which has in our case $\mathrm{Re}(\omega) = -0.197$. The computations are done for a toroidal mode number $n = -1$ and poloidal mode number $m = [-1, 5]$. The mode is resistively damped by resonant interaction with the MHD continua. The η-convergence study of this TFAE mode is shown in Fig. 6a, similar to [41]. This study shows that the TFAE damping rate $\mathrm{Im}(\omega) \approx -1.4 \times 10^{-4}$. Furthermore, one needs at least 801 grid points to reach convergence. The $\sqrt{\Psi}$-dependence of the perturbed normal velocity for three different poloidal mode numbers has been plotted in Fig. 6b. This shows that the $m = 2$ harmonic is the most dominant one. The near singular behaviour at $\sqrt{\Psi} \approx 0.90$ is due to the interaction with the MHD continua.

4.4. MHD continua in the presence of toroidal rotation and gravity

The following example shows that FINESSE and PHOENIX can also be used for astrophysical applications, like a stability analysis of a two-dimensional accretion torus or disk. Our accretion disk is an axisymmetric torus of fixed cross-sectional shape, within which a two-dimensional equilibrium with toroidal flow and gravity has been constructed. For this case, we specify the equations which the FINESSE code solves, namely

$$R\frac{\partial}{\partial R}\left(\frac{1}{R}\frac{\partial \Psi}{\partial R}\right) + \frac{\partial^2 \Psi}{\partial Z^2} = -\frac{1}{2}\frac{\mathrm{d}I^2}{\mathrm{d}\Psi} - R^2\frac{\partial p}{\partial \Psi}, \tag{52}$$

$$\left.\frac{\partial p}{\partial R}\right|_{\Psi=\mathrm{const}} = \rho R\Omega^2 - \rho\frac{\partial \Phi_{\mathrm{grav}}}{\partial R}, \tag{53}$$

$$\left.\frac{\partial p}{\partial Z}\right|_{\Psi=\mathrm{const}} = -\rho\frac{\partial \Phi_{\mathrm{grav}}}{\partial Z}, \tag{54}$$

where the Newtonian gravitational potential $\Phi_{\mathrm{grav}} = -GM_*/\sqrt{R^2 + Z^2}$. The latter two equations can be solved analytically under the assumption that the density, the temperature or the entropy is a flux functions. All three cases are currently implemented in the FINESSE code.

For this example the density is assumed to be a flux function. For the equilibrium the following flux functions have been used:

$$\begin{aligned} I^2(\Psi) &= A(1 - 0.0385\Psi + 0.02\Psi^2 + 0.00045\Psi^3), \quad \rho(\Psi) = 1, \\ p_0(\Psi) &= AB(1 - 0.9\Psi), \quad \Omega(\Psi) = C(1 - 0.9\Psi), \end{aligned} \tag{55}$$

where $A = 112$, $B = 0.01$ and $C = 0.1$. The cross-section of the accretion disk is circular and we used an inverse aspect ratio $\epsilon = 0.1$. The plasma beta $\beta = 2p/B^2$ increases monotonically from 0.63 at the inner part to 0.76 at the outer part of the disk. The ratio of the toroidal velocity to the Keplerian velocity is in the range $v_\varphi/v_{\mathrm{Kepler}} = [0.085; 1.049]$. The minimum value correspond to boundary locations close to the last closed flux surface while the maximum value is reached close to the centre of the accretion disk. Furthermore, the gravitational potential on the magnetic axis $GM_*/R_{\mathrm{M}} = -0.35$. This value has been scaled with respect to

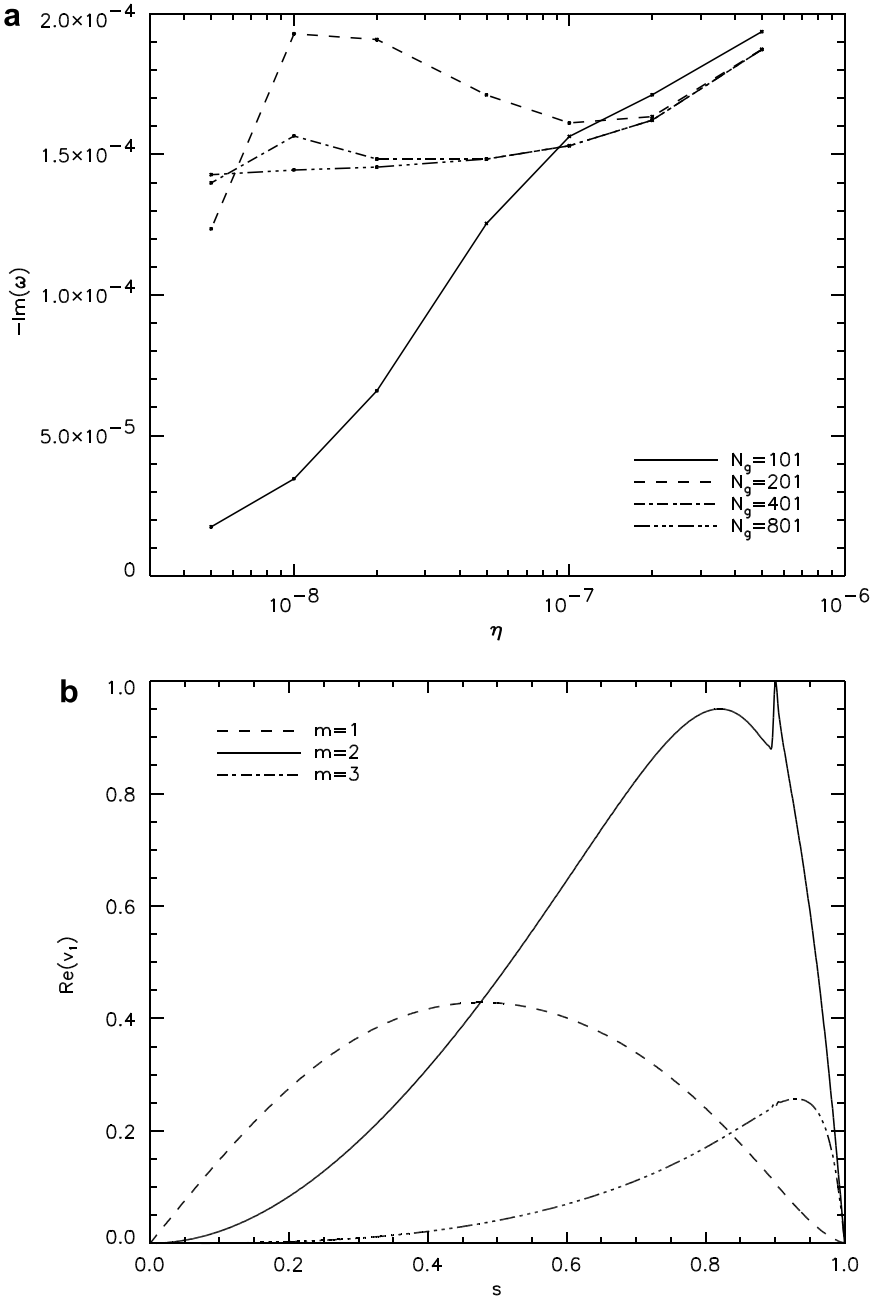

Fig. 6. (a) Continuum damping of the flow-induced global gap mode, and (b) the normal component of the perturbed velocity as function of the radial flux coordinate $s \equiv \sqrt{\Psi}$; $\eta = 5 \times 10^{-8}, N_g = 801, m = [-1, 5]$.

the Alfvén speed on the magnetic axis. For the computations, a toroidal mode number $n = -1$ and poloidal mode numbers $m = [-3, 5]$ have been used. Fig. 7 shows the sub-spectrum of the MHD continua. From plot (b) and (c) it is clear that in this case the MHD continua contain overstable modes. These modes appear due to the presence of toroidal rotation and gravity in a manner similar to the unstable continua for toroidally rotating tokamak equilibria studied by van der Holst et al. [32]. A systematic investigation of the influence of the gravity on these MHD continua is currently ongoing.

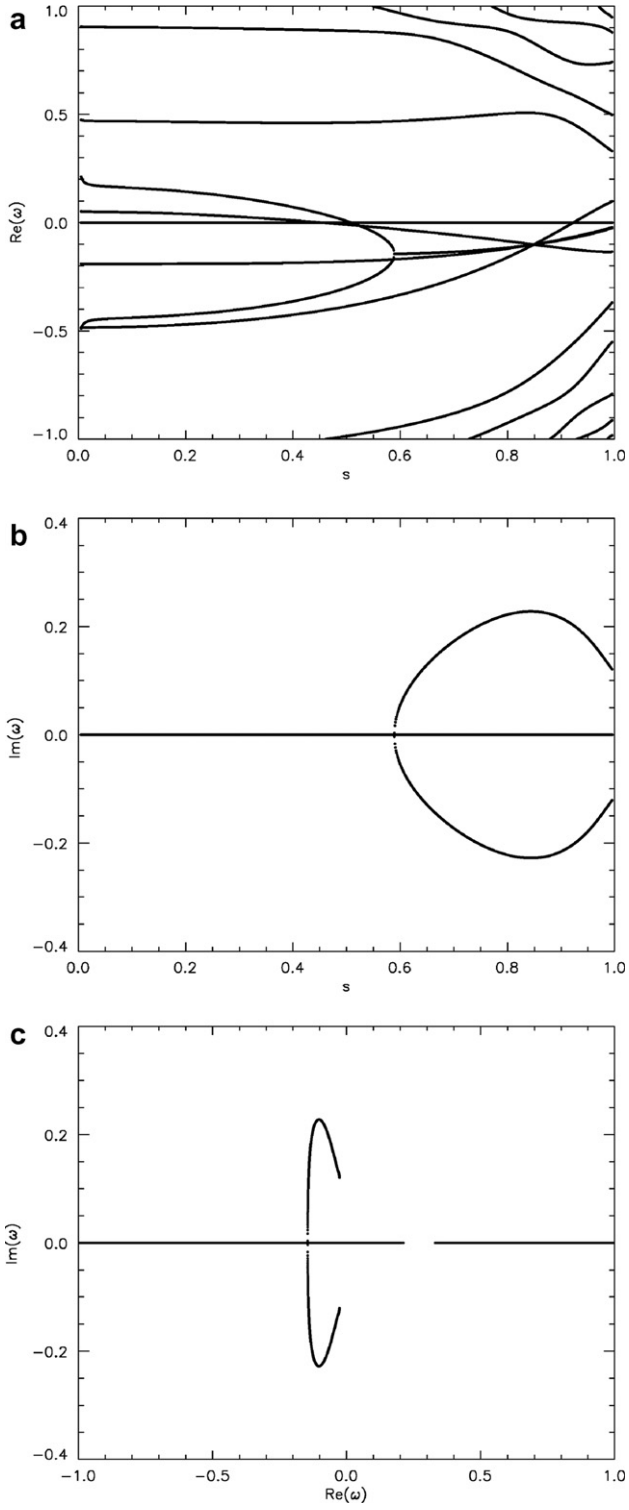

Fig. 7. Real (a), and imaginary (b) parts of the subspectrum of the MHD continua as function of the radial flux coordinate $s \equiv \sqrt{\Psi}$ and (c) subspectrum of the MHD continua in the complex plane for a toroidal mode number $n = -1$ and poloidal mode numbers $m = [-3, 5]$. Overstable continuum modes in accretion disks exist due to the presence of toroidal flow and a strong gravitational field.

4.5. Localized gap modes in the presence of toroidal and poloidal flow

In this section we present spectral results of localized modes which appear inside the gap of the continuous spectrum. This is done for an equilibrium which contains dynamical effects due to both toroidal and poloidal flow. For the tokamak equilibrium we used the following flux flunctions:

$$\begin{aligned}
&\Lambda_1 = A \times (1 - 0.4\Psi + 0.2\Psi^2),\\
&\Lambda_2 A \times 1 \times 10^{-3} \times (1 - 1.6\Psi + 0.8\Psi^2),\\
&\Lambda_3 = A \times 1 \times 10^{-4},\\
&\Lambda_4 = 5 \times 10^2,\\
&\Lambda_5 = A \times 0 \times (1 - 0.85\Psi),
\end{aligned} \tag{56}$$

where $A = 0.142$ and the Λ_i's are the same flux functions as those defined in the FINESSE paper [2]. Furthermore, the tokamak has a circular cross-section and an inverse aspect ratio $\epsilon = 0.05$. The solutions of the algebraic equation for the squared Alfvén Mach number M^2 are selected in the slow flow domain, i.e. the next elliptic flow regime. The computation of the continuous MHD spectrum and the localized gap modes are done for a toroidal mode number $n = -1$ and poloidal mode numbers $m = [-1, 5]$. Fig. 8 shows a part of the continuous MHD spectrum, which has a $|\Delta m| = 1$ gap in the Alfvén spectra at $s \approx 0.82$. In this gap there are indications of a cluster sequence of ideal localized gap modes, which were found to follow anti-Sturmian properties. For one-dimensional problems, Sturmian and anti-Sturmian behaviour can be proven using the oscillation theorem (Goedbloed and Sakanaka [20]). The zeroth and the second gap mode found here are shown in Fig. 9 which have an eigenfrequency of $\omega = -0.5088$ and $\omega = -0.5072$, respectively. The eigenfequency of the first gap mode, not shown in a figure, is $\omega = -0.5080$. Fig. 9 shows that the $m = 1$ and $m = 2$ harmonics are the dominant ones. These localized modes seem to cluster towards the extremum of one of the Alfvén continuum branches.

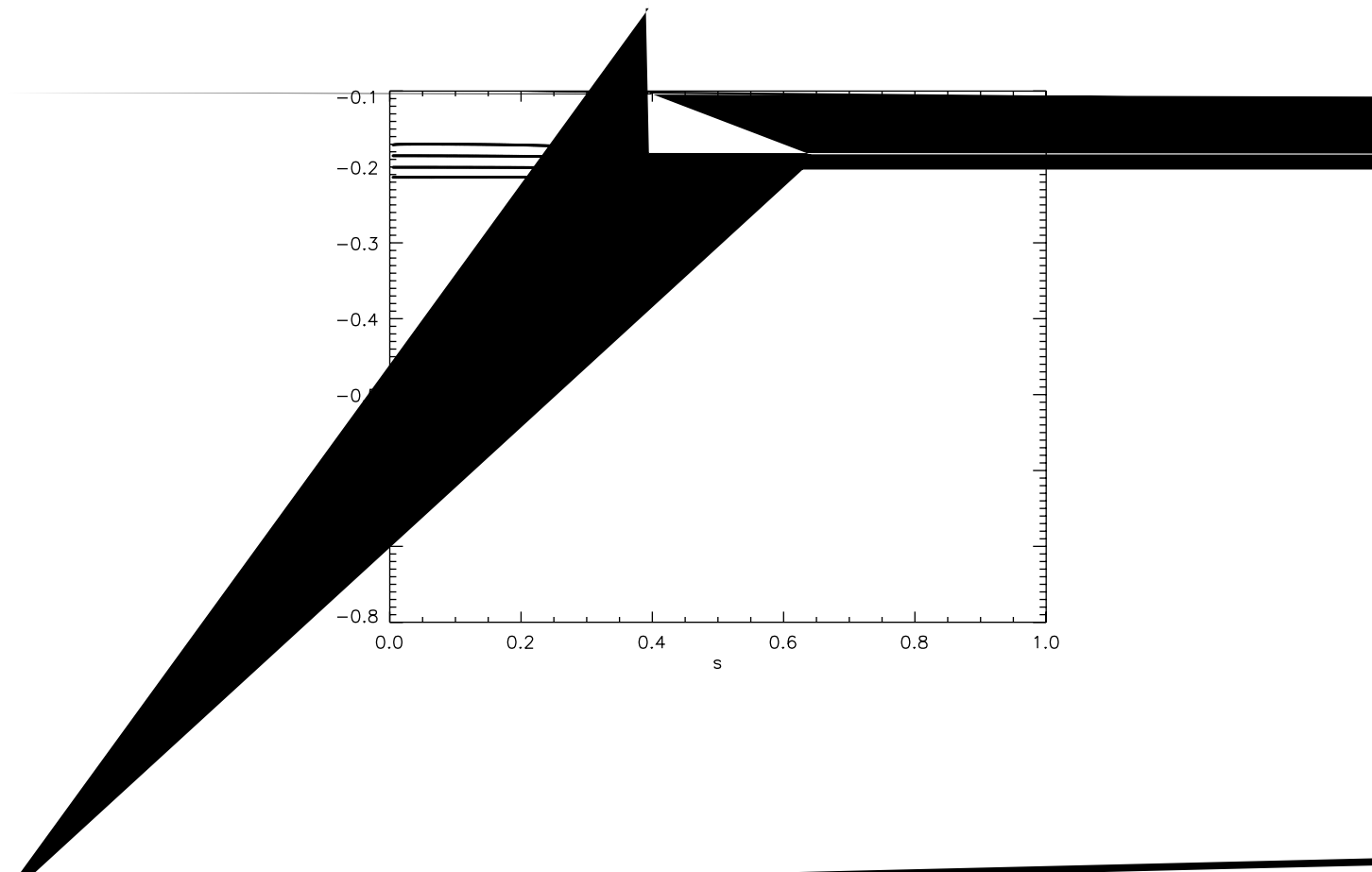

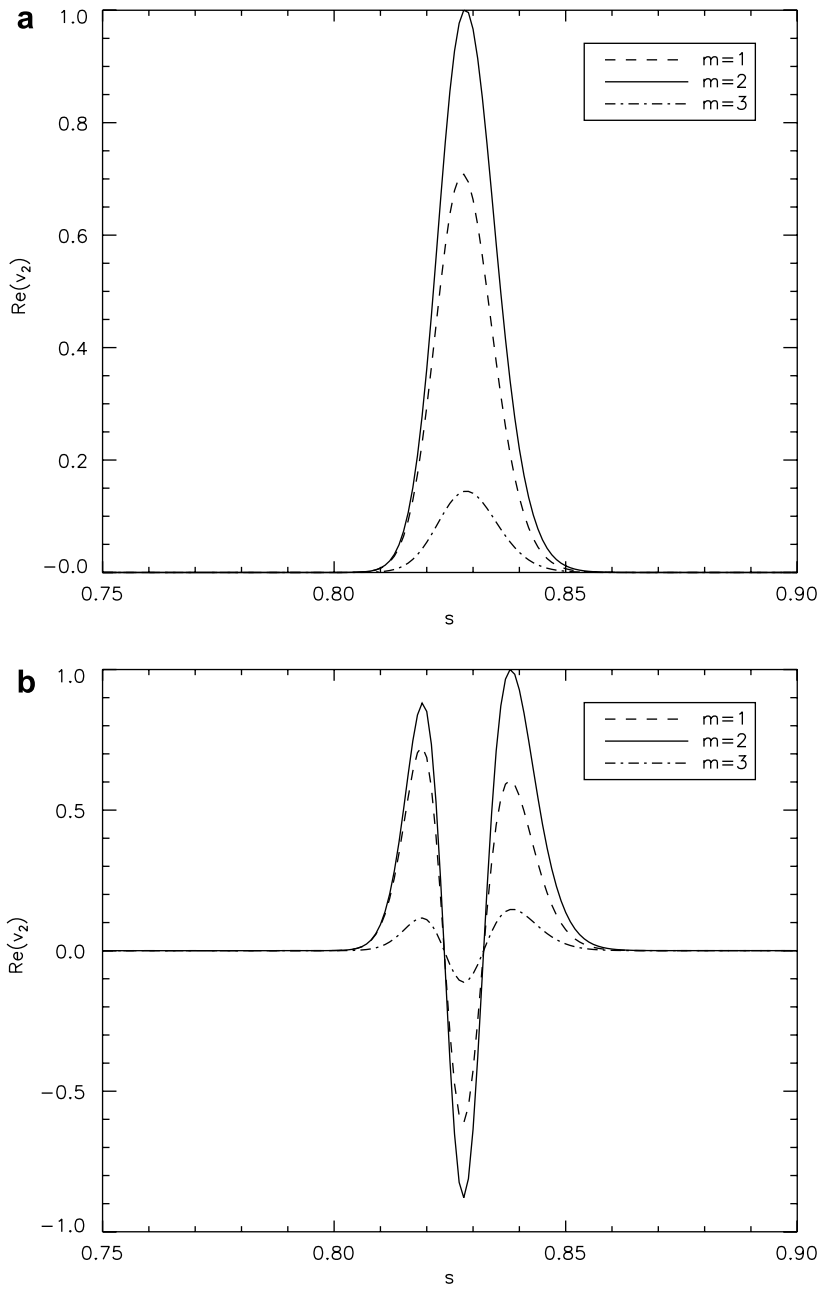

Fig. 9. The tangential component of the perturbed velocity (a) of the zeroth gap mode with eigenfrequency $\omega = -0.5088$, and (b) of the second gap mode with eigenfrequency $\omega = -0.5072$ as function of the radial flux coordinate $s \equiv \sqrt{\Psi}$; $N_g = 1001, m = [-1, 5]$.

4.6. MHD continua for gravity dominated accretion disks with toroidal and poloidal flow

In this last example we show that the PHOENIX code is able to compute the full MHD continua in the presence of toroidal and poloidal flow and gravity. To demonstrate this, equilibrium C of the paper by Goedbloed et al. [17] has been used. The flux functions specified in this paper have also been implemented into the FINESSE code. For the toroidal and poloidal mode numbers we used the same ones as specified in the paper, which are a toroidal mode number $n = -1$ and poloidal mode numbers $m = [-2, 6]$. A part of the MHD continuous spectrum is shown in Fig. 10, which reproduces Fig. 13 presented by Goedbloed et al. [17] where a

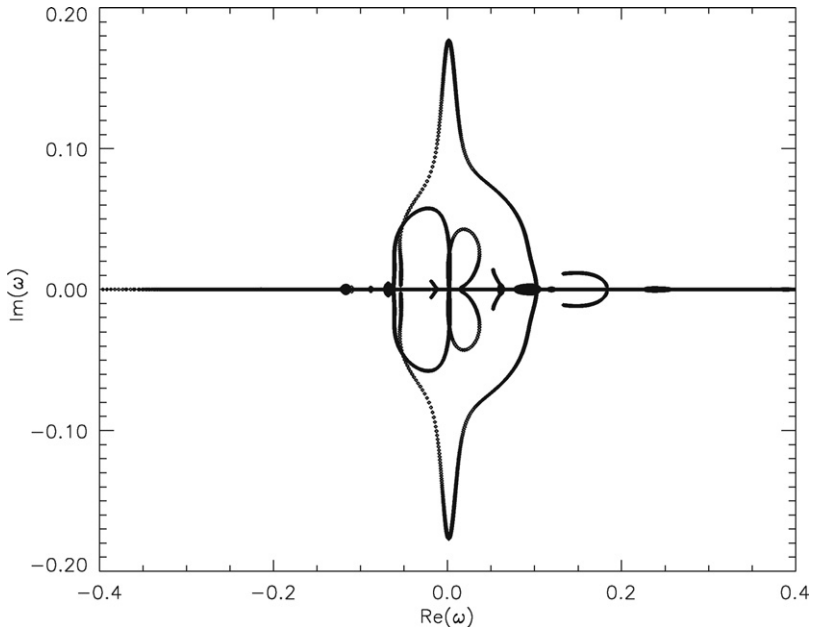

Fig. 10. Subspectrum of the MHD continua in the complex plane for a toroidal mode number $n = -1$ and poloidal mode numbers $m = [-2, 6]$.

detailed explanation of this spectrum is given. Part of the continuous modes become overstable or unstable due to a six-fold coupling scheme between Alfvén and slow continua branches of neighboring poloidal modes numbers m. This can occur at every rational q-surface. The presence of large, "transonic" poloidal flow and strong gravitational field causes mode-locking and leads to violent instabilities with very localized eigenfunctions.

5. Conclusions

The ideal or resistive MHD spectrum for tokamaks or accretion disks can be computed by the PHOENIX code. The stationary MHD equilibrium considered may include purely toroidal flow or both toroidal and poloidal flow. The numerical computations are done in a specific flux-coordinate system and make use of an appropriate choice for the projection of the perturbed velocity and perturbed vector potential. A mixed Fourier and finite element method has been used for the discretization which results in a large-scale non-Hermitian general eigenvalue problem. This generalized eigenvalue problem is solved using the iterative Jacobi–Davidson algorithm.

The test results for a Soloviev equilibrium show excellent agreement, typically within 1%, with other existing MHD spectral codes. We included a new reference test case with purely toroidal flow demonstrating that the flow has a stabilizing effect on the particular unstable mode computed regardless of the direction of the flow. The resistive internal kink mode has been computed for different values of the resistivity. These computations show that the code can accurately handle small values for the resistivity at least down to 10^{-11}. The code reproduced the Toroidal Flow induced Alfvén Eigenmode [31], which demonstrates that the code can accurately handle cases with resistivity and flow effects occuring simultaneously.

For a tokamak plasma in the presence of toroidal and poloidal flow localized gap modes have been presented. These ideal gap modes appear to cluster to the local extremum of one of the branches of the MHD continua.

For an accretion torus or disk two cases where the MHD continua have been calculated are presented in detail. Both are stratified due to the presence of a central object in the origin of the surrounding torus where one example considered purely toroidal flow and the other one both toroidal and poloidal flow. Both show that the MHD continua can contain unstable and overstable modes due to the presence of (strong) gravitational fields in combination with equilibrium flow-driven dynamics. Currently, an investigation is ongoing

on the influence of gravity on the MHD continua in the case of equilibria with purely toroidal flow. Future work will be done on the localized gap modes in the presence of toroidal and poloidal flow. This will be done numerically as well as analytically.

Acknowledgments

This work was carried out within the framework of the European Fusion Programme, supported by the European Communities under contract of the Association between EURATOM/FOM. Views and opinions expressed herein do not necessarily reflect those of the European Commission. This work is part of the research programme of the "Stichting voor Fundamenteel Onderzoek der Materie (FOM)", which is financially supported by the "Nederlandse Organisatie voor Wetenschappelijk Onderzoek (NWO)".

Appendix A. Equilibrium with purely toroidal flow with or without gravity

For the equilibrium with purely toroidal flow we neglect the time-derivative in the momentum Eq. (2). This equation is then projected in three different ways, namely in the toroidal direction, parallel, and perpendicular to the poloidal magnetic field. The toroidal projection reveals that the poloidal stream function $I \equiv RB_\varphi$ is a flux function, i.e. $I = I(\Psi)$. The projection parallel to the poloidal magnetic field leads to two equations,

$$\begin{aligned} \left.\frac{\partial p}{\partial R}\right|_{\Psi=\text{const}} &= \rho\left(R\Omega^2 - \frac{\partial \Phi}{\partial R}\right), \\ \left.\frac{\partial p}{\partial Z}\right|_{\Psi=\text{const}} &= -\rho\frac{\partial \Phi}{\partial Z}, \end{aligned} \tag{A.1}$$

where the pressure $p = p(\Psi; R, Z)$. The last projection, perpendicular to the poloidal magnetic field, results in the extended Grad–Shafranov equation,

$$R^2\nabla\cdot\left(\frac{1}{R^2}\nabla\Psi\right) = -I\frac{\mathrm{d}I}{\mathrm{d}\Psi} - R^2\frac{\partial p}{\partial \Psi}. \tag{A.2}$$

The two equations parallel to the poloidal magnetic field (A.1) can be solved analytically under the assumption that the temperature T, the density ρ or the entropy $S = p\rho^{-\gamma}$ is a flux function. The temperature can be assumed constant on a flux surface due to the high thermal conductivity along the field lines. This assumption is valid at least on transport time scales, which is long compared to the Alfvén time. In this case, the pressure reads

$$p(\Psi; R, Z) = p_0(\Psi)\exp\left[(R^2 - R_0^2)\Lambda_T(\Psi) - \frac{\Phi(R,Z)}{T(\Psi)}\right], \tag{A.3}$$

where $\Lambda_T \equiv \Omega^2/(2T)$ and R_0 is the geometric axis of the tokamak or accretion disk. The flux function p_0 corresponds to the pressure for a static equilibrium without gravity. The extended Grad–Shafranov equation (A.2) reduces to

$$R^2\nabla\cdot\left(\frac{1}{R^2}\nabla\Psi\right) = -I\frac{\mathrm{d}I}{\mathrm{d}\Psi} - R^2\left\{\frac{\mathrm{d}p_0}{\mathrm{d}\Psi} + p_0\left[(R^2 - R_0^2)\frac{\mathrm{d}\Lambda_T}{\mathrm{d}\Psi} + \frac{\Phi}{T^2}\frac{\mathrm{d}T}{\mathrm{d}\Psi}\right]\right\}\exp\left[\left(R^2 - R_0^2\right)\Lambda_T - \frac{\Phi}{T}\right]. \tag{A.4}$$

However, on MHD time scales, it also possible to assume $\rho = \rho(\Psi)$. Using this assumption, the pressure can be written as

$$p(\Psi; R, Z) = p_0(\Psi)\left[1 + (R^2 - R_0^2)\Lambda_\rho(\Psi) - \frac{\Phi(R,Z)}{T_\rho(\Psi)}\right], \tag{A.5}$$

where the quasi-temperature $T_\rho \equiv p_0/\rho$ and $\Lambda_\rho \equiv \Omega^2/(2T_\rho)$. In this case the extended Grad–Shafranov equation (A.2) can be written as

$$\begin{aligned} R^2\nabla\cdot\left(\frac{1}{R^2}\nabla\Psi\right) = &-I\frac{\mathrm{d}I}{\mathrm{d}\Psi} - R^2\left\{\frac{\mathrm{d}p_0}{\mathrm{d}\Psi} + p_0\left[(R^2 - R_0^2)\frac{\mathrm{d}\Lambda_\rho}{\mathrm{d}\Psi} + \frac{\Phi}{T_\rho^2}\frac{\mathrm{d}T_\rho}{\mathrm{d}\Psi}\right]\left[1 + (R^2 - R_0^2)\Lambda_\rho - \frac{\Phi}{T_\rho}\right]^{-1}\right\} \\ &\times\left[1 + (R^2 - R_0^2)\Lambda_\rho - \frac{\Phi}{T_\rho}\right]. \end{aligned} \tag{A.6}$$

The last case is under the assumption that the entropy S is a flux function. This assumption has the advantage that it permits a natural extension to toroidal and poloidol flows, where the entropy has to be a flux function (Zehrfeld et al. [54] and Hameiri [29]). In this case the pressure reads

$$p(\Psi;R,Z)=p_0(\Psi)\left\{1+\frac{\gamma-1}{\gamma}\left[(R^2-R_0^2)\Lambda_S(\Psi)-\frac{\Phi(R,Z)}{T_S(\Psi)}\right]\right\}^{\gamma/(\gamma-1)} \tag{A.7}$$

and the extended Grad–Shafranov equation (A.2) reduces to

$$\begin{aligned}R^2\nabla\cdot\left(\frac{1}{R^2}\nabla\Psi\right)=&-I\frac{\mathrm{d}I}{\mathrm{d}\Psi}-R^2\left\{\frac{\mathrm{d}p_0}{\mathrm{d}\Psi}+p_0\left[(R^2-R_0^2)\frac{\mathrm{d}\Lambda_S}{\mathrm{d}\Psi}+\frac{\Phi}{T_S^2}\frac{\mathrm{d}T_S}{\mathrm{d}\Psi}\right]\left[1+\frac{\gamma-1}{\gamma}\left((R^2-R_0^2)\Lambda_S-\frac{\Phi}{T_S}\right)\right]^{-1}\right\}\\&\times\left\{1+\frac{\gamma-1}{\gamma}\left[(R^2-R_0^2)\Lambda_S-\frac{\Phi}{T_S}\right]\right\}^{\gamma/(\gamma-1)},\end{aligned} \tag{A.8}$$

where the quasi-temperature $T_S\equiv S\rho_0^{\gamma-1}$ and $\Lambda_S\equiv\Omega^2/(2T_S)$.

The extended Grad–Shafranov equation without gravity of the first two cases have been published by van der Holst et al. [32]. For the three cases the density can be easily derived by inserting the corresponding pressure back into the momentum equations parallel to the poloidal magnetic field (A.1). The density can then be written as

$$\rho(\Psi;R,Z)=\rho_0(\Psi)\times\begin{cases}\left[\left(R^2-R_0^2\right)\Lambda_T-\frac{\Phi}{T}\right]\\1\\\left\{1+\frac{\gamma-1}{\gamma}\left[\left(R^2-R_0^2\right)\Lambda_S-\frac{\Phi}{T_S}\right]\right\}^{1/(\gamma-1)}\end{cases} \tag{A.9}$$

for the temperature, density or entropy as flux function, respectively. Here, the flux function ρ_0 is the density in the case of a static equilibrium without gravity.

Appendix B. Matrix elements

For comparison with the matrix elements used in the CASTOR code [37] for spectral diagnosis of static equilibria, we list the matrix elements as occuring for stationary equilibria with toroidal and poloidal flow and external gravity. The matrix elements of the matrix $\mathbf{B}$ are:

$$\begin{aligned}
B(1,1)&=hh\cdot\frac{fJ}{s^2}, & B(4,3)&=hh\cdot g_{22}\frac{\rho_0 J}{f},\\
B(2,2)&=HH\cdot g_{11}\frac{\rho_0 J}{f}, & B(4,4)&=hh\cdot(g_{22}+q^2R^2)\frac{\rho_0 J}{f},\\
B(2,3)&=Hh\cdot -\mathrm{i}g_{12}\frac{\rho_0 J}{f}, & B(5,5)&=hh\cdot\frac{f\rho_0 J}{s^2},\\
B(2,4)&=Hh\cdot -\mathrm{i}g_{12}\frac{\rho_0 J}{f}, & B(6,6)&=hh\cdot g_{22}\frac{R^2}{fJ},\\
B(3,2)&=hH\cdot \mathrm{i}g_{12}\frac{\rho_0 J}{f}, & B(6,7)&=hH\cdot -\mathrm{i}g_{12}\frac{R^2}{fJ},\\
B(3,3)&=hh\cdot g_{22}\frac{\rho_0 J}{f}, & B(7,6)&=Hh\cdot \mathrm{i}g_{12}\frac{R^2}{fJ},\\
B(3,4)&=hh\cdot g_{22}\frac{\rho_0 J}{f}, & B(7,7)&=HH\cdot g_{11}\frac{R^2}{fJ},\\
B(4,2)&=hH\cdot \mathrm{i}g_{12}\frac{\rho_0 J}{f}, & B(8,8)&=HH\cdot\frac{fJ}{R^2},
\end{aligned}$$

and the elements of the matrix **A** are:

$$
\begin{aligned}
A(1,1) &= hh\cdot -\mathrm{i}\frac{f}{s^2}\left\{\chi'\left[m'\frac{1}{\rho_0}-\mathrm{i}\frac{\partial}{\partial\vartheta}\left(\frac{1}{\rho_0}\right)\right]+nJ\frac{V_\varphi}{R}\right\},\\
A(1,2) &= hH'\cdot -\frac{\rho_0 J}{s}+hH\cdot -\frac{1}{s}\frac{\partial}{\partial s}(\rho_0 J),\\
A(1,3) &= hh\cdot\frac{1}{s}\left[\mathrm{i}\frac{\partial}{\partial\vartheta}(\rho_0 J)-m'\rho_0 J\right],\\
A(1,4) &= hh\cdot\frac{1}{s}\left[\mathrm{i}\frac{\partial}{\partial\vartheta}(\rho_0 J)-(m'+nq)\rho_0 J\right],\\
A(2,1) &= H'h\cdot\frac{T_0 J}{s}+Hh\cdot\frac{1}{s}\left\{T_0\frac{\partial J}{\partial s}-J\frac{\partial\Phi_{\mathrm{grav}}}{\partial s}-\chi'^2\left[\frac{1}{\rho_0}\frac{\partial}{\partial\vartheta}\left(\frac{g_{12}}{\rho_0 J}\right)-\frac{1}{2}\frac{1}{\rho_0^2 J}\frac{\partial g_{22}}{\partial s}\right]+\frac{1}{2}J\left(\frac{V_\varphi}{R}\right)^2\frac{\partial R^2}{\partial s}\right\},\\
A(2,2) &= HH\cdot\frac{-1}{f}\left[\mathrm{i}\chi'\left(-\mathrm{i}\frac{\partial g_{11}}{\partial\vartheta}+m'g_{11}\right)+g_{12}\frac{\partial\chi'}{\partial s}-\chi'\frac{g_{12}}{\rho_0 J}\frac{\partial}{\partial s}(\rho_0 J)+\mathrm{i}ng_{11}\rho_0 J\frac{V_\varphi}{R}\right],\\
A(2,3) &= Hh\cdot\frac{-1}{f}\left\{\chi'\left[m'g_{12}-\mathrm{i}\frac{\partial g_{12}}{\partial\vartheta}-\mathrm{i}\rho_0 J\frac{\partial}{\partial\vartheta}\left(\frac{g_{12}}{\rho_0 J}\right)+\mathrm{i}\frac{\partial g_{22}}{\partial s}\right]+ng_{12}\rho_0 J\frac{V_\varphi}{R}\right\},\\
A(2,4) &= Hh\cdot\frac{-1}{f}\left\{\chi'\left[m'g_{12}-\mathrm{i}\frac{\partial g_{12}}{\partial\vartheta}-\mathrm{i}\rho_0 J\frac{\partial}{\partial\vartheta}\left(\frac{g_{12}}{\rho_0 J}\right)+\mathrm{i}\frac{\partial g_{22}}{\partial s}\right]+ng_{12}\rho_0 J\frac{V_\varphi}{R}+\mathrm{i}q\rho_0 J\frac{V_\varphi}{R}\frac{\partial R^2}{\partial s}\right\},\\
A(2,5) &= H'h\cdot\frac{\rho_0 J}{s}+Hh\cdot\frac{\rho_0}{s}\frac{\partial J}{\partial s},\\
A(2,6) &= H'h\cdot\frac{1}{f}\left(n\frac{g_{22}}{J}-m'q\frac{R^2}{J}\right)+Hh\cdot\frac{1}{f}\left[m'q\frac{\partial}{\partial s}\left(\frac{R^2}{J}\right)-n\frac{\partial}{\partial s}\left(\frac{g_{22}}{J}\right)+\mathrm{i}n\frac{g_{12}}{J}(m'+nq)+2n\frac{\partial}{\partial\vartheta}\left(\frac{g_{12}}{J}\right)\right],\\
A(2,7) &= H'H'\cdot\frac{q}{f}\frac{R^2}{J}+H'H\cdot -\frac{\mathrm{i}n}{f}\frac{g_{12}}{J}+HH'\cdot\frac{-q}{f}\frac{\partial}{\partial s}\left(\frac{R^2}{J}\right)+HH\cdot\frac{n}{f}\left[\frac{g_{11}}{J}(m'+nq)-\mathrm{i}\frac{\partial}{\partial\vartheta}\left(\frac{g_{11}}{J}\right)\right],\\
A(2,8) &= H'H'\cdot\frac{-1}{f}\frac{g_{22}}{J}+H'H\cdot\frac{\mathrm{i}m'}{f}\frac{g_{12}}{J}+HH'\cdot\frac{1}{f}\left[\frac{\partial}{\partial s}\left(\frac{g_{22}}{J}\right)-\mathrm{i}\frac{g_{12}}{J}(m'+nq)-2\frac{\partial}{\partial\vartheta}\left(\frac{g_{12}}{J}\right)\right]\\
&\quad +HH\cdot\frac{-m'}{f}\left[\frac{g_{11}}{J}(m'+nq)-\mathrm{i}\frac{\partial}{\partial\vartheta}\left(\frac{g_{11}}{J}\right)\right],\\
A(3,1) &= hh\cdot\frac{1}{s}\left[mT_0 J+\mathrm{i}T_0\frac{\partial J}{\partial\vartheta}-\mathrm{i}J\frac{\partial\Phi_{\mathrm{grav}}}{\partial\vartheta}-\frac{1}{2}\mathrm{i}\chi'^2 J\frac{\partial}{\partial\vartheta}\left(\frac{g_{22}}{\rho_0^2 J^2}\right)+\frac{1}{2}\mathrm{i}J\left(\frac{V_\varphi}{R}\right)^2\frac{\partial R^2}{\partial\vartheta}\right],\\
A(3,2) &= hH\cdot\frac{1}{f}\left\{\chi'\left[m'g_{12}-\mathrm{i}\rho_0 J\frac{\partial}{\partial s}\left(\frac{g_{22}}{\rho_0 J}\right)\right]-\mathrm{i}g_{22}\frac{\partial\chi'}{\partial s}+ng_{12}\rho_0 J\frac{V_\varphi}{R}\right\},\\
A(3,3) &= hh\cdot\frac{-1}{f}\left\{\chi'\left[\mathrm{i}m'g_{22}+\rho_0 J\frac{\partial}{\partial\vartheta}\left(\frac{g_{22}}{\rho_0 J}\right)\right]+\mathrm{i}ng_{22}\rho_0 J\frac{V_\varphi}{R}\right\},\\
A(3,4) &= hh\cdot\frac{-1}{f}\left\{\chi'\left[\mathrm{i}m'g_{22}+\rho_0 J\frac{\partial}{\partial\vartheta}\left(\frac{g_{22}}{\rho_0 J}\right)\right]+\mathrm{i}ng_{22}\rho_0 J\frac{V_\varphi}{R}-q\rho_0 J\frac{V_\varphi}{R}\frac{\partial R^2}{\partial\vartheta}\right\},\\
A(3,5) &= hh\cdot\frac{1}{s}\left(m\rho_0 J+\mathrm{i}\rho_0\frac{\partial J}{\partial\vartheta}\right),\\
A(3,6) &= hh\cdot\frac{1}{f}\left[-n\frac{g_{22}}{J}(m'-m+nq)+\mathrm{i}n\frac{\partial}{\partial\vartheta}\left(\frac{g_{22}}{J}\right)-mm'q\frac{R^2}{J}+\mathrm{i}m'q\frac{\partial}{\partial\vartheta}\left(\frac{R^2}{J}\right)\right],\\
A(3,7) &= hH'\cdot\frac{q}{f}\left[m\frac{R^2}{J}-\mathrm{i}\frac{\partial}{\partial\vartheta}\left(\frac{R^2}{J}\right)\right]+hH\cdot\frac{n}{f}\left[\mathrm{i}\frac{g_{12}}{J}(m'-m+nq)+\frac{\partial}{\partial s}\left(\frac{g_{22}}{J}\right)\right],\\
A(3,8) &= hH'\cdot\frac{1}{f}\left[\frac{g_{22}}{J}(m'-m+nq)-\mathrm{i}\frac{\partial}{\partial\vartheta}\left(\frac{g_{22}}{J}\right)\right]+hH\cdot\frac{-m'}{f}\left[\mathrm{i}\frac{g_{12}}{J}(m'-m+nq)+\frac{\partial}{\partial s}\left(\frac{g_{22}}{J}\right)\right],
\end{aligned}
$$

$$A(4,1) = hh\cdot\frac{1}{s}\left[(m+nq)T_0J + \mathrm{i}T_0\frac{\partial J}{\partial\vartheta} - \frac{1}{2}\mathrm{i}\chi'^2J\frac{\partial}{\partial\vartheta}\left(\frac{g_{22}}{\rho_0^2J^2}\right) + \frac{1}{2}\mathrm{i}J\left(\frac{V_\varphi}{R}\right)^2\frac{\partial R^2}{\partial\vartheta} - \mathrm{i}q\chi'\frac{1}{\rho_0}\frac{\partial}{\partial\vartheta}(RV_\varphi) - \mathrm{i}J\frac{\partial\Phi_{\mathrm{grav}}}{\partial\vartheta}\right],$$

$$A(4,2) = hH\cdot\frac{-1}{f}\left\{\chi'\left[-m'g_{12} + \mathrm{i}\rho_0J\frac{\partial}{\partial s}\left(\frac{g_{22}}{\rho_0J}\right)\right] + \mathrm{i}g_{22}\frac{\partial\chi'}{\partial s} - ng_{12}\rho_0J\frac{V_\varphi}{R} + \mathrm{i}q\rho_0J\frac{\partial}{\partial s}(RV_\varphi)\right\},$$

$$A(4,3) = hh\cdot\frac{-1}{f}\left\{\chi'\left[\mathrm{i}m'g_{22} + \rho_0J\frac{\partial}{\partial\vartheta}\left(\frac{g_{22}}{\rho_0J}\right)\right] + \mathrm{i}ng_{22}\rho_0J\frac{V_\varphi}{R} + q\rho_0J\frac{\partial}{\partial\vartheta}(RV_\varphi)\right\},$$

$$A(4,4) = hh\cdot\frac{-1}{f}\left\{\chi'\left[\mathrm{i}m'(g_{22}+q^2R^2) + \rho_0J\frac{\partial}{\partial\vartheta}\left(\frac{g_{22}}{\rho_0J}\right) + q^2\frac{\partial R^2}{\partial\vartheta}\right] + \mathrm{i}n\rho_0J(g_{22}+q^2R^2)\frac{V_\varphi}{R} + q\rho_0JR^2\frac{\partial}{\partial\vartheta}\left(\frac{V_\varphi}{R}\right)\right\},$$

$$A(4,5) = hh\cdot\frac{1}{s}\left[(m+nq)\rho_0J + \mathrm{i}\rho_0\frac{\partial J}{\partial\vartheta}\right],$$

$$A(4,6) = hh\cdot\frac{1}{f}\left[n\frac{g_{22}}{J}(m-m') + \mathrm{i}n\frac{\partial}{\partial\vartheta}\left(\frac{g_{22}}{J}\right) + m'q\frac{R^2}{J}(m'-m) + \mathrm{i}nq^2\frac{\partial}{\partial\vartheta}\left(\frac{R^2}{J}\right)\right],$$

$$A(4,7) = hH'\cdot\frac{q}{f}\frac{R^2}{J}(m-m') + hH\cdot\frac{n}{f}\left[\mathrm{i}\frac{g_{12}}{J}(m'-m) + \frac{\partial}{\partial s}\left(\frac{g_{22}}{J}\right) + q\frac{\partial}{\partial s}(RB_\varphi)\right],$$

$$A(4,8) = hH'\cdot\frac{1}{f}\left[\frac{g_{22}}{J}(m'-m) - \mathrm{i}\frac{\partial}{\partial\vartheta}\left(\frac{g_{22}}{J}\right) - \mathrm{i}q^2\frac{\partial}{\partial\vartheta}\left(\frac{R^2}{J}\right)\right] + hH\cdot\frac{m'}{f}\left[\mathrm{i}(m-m')\frac{g_{12}}{J} - \frac{\partial}{\partial s}\left(\frac{g_{22}}{J}\right) - q\frac{\partial}{\partial s}(RB_\varphi)\right],$$

$$A(5,1) = hh\cdot-\frac{f}{s^2}\chi'\left[\frac{1}{\rho_0}\frac{\partial T_0}{\partial\vartheta} + (\gamma-1)T_0\frac{\partial}{\partial\vartheta}\left(\frac{1}{\rho_0}\right)\right],$$

$$A(5,2) = hH'\cdot-(\gamma-1)\frac{p_0J}{s} + hH\cdot-\frac{1}{s}\left[\rho_0J\frac{\partial T_0}{\partial s} + (\gamma-1)p_0\frac{\partial J}{\partial s}\right],$$

$$A(5,3) = hh\cdot\frac{1}{s}\left[\mathrm{i}\rho_0J\frac{\partial T_0}{\partial\vartheta} - (\gamma-1)\left(m'p_0J - \mathrm{i}p_0\frac{\partial J}{\partial\vartheta}\right)\right],$$

$$A(5,4) = hh\cdot\frac{1}{s}\left\{\mathrm{i}\rho_0J\frac{\partial T_0}{\partial\vartheta} - (\gamma-1)\left[(m'+nq)p_0J - \mathrm{i}p_0\frac{\partial J}{\partial\vartheta}\right]\right\},$$

$$A(5,5) = hh\cdot-\frac{f}{s^2}\left\{\chi'\left[\mathrm{i}m' - (\gamma-1)\frac{1}{\rho_0}\frac{\partial\rho_0}{\partial\vartheta}\right] + \mathrm{i}n\rho_0J\frac{V_\varphi}{R}\right\},$$

$$A(6,2) = hH\cdot\mathrm{i}g_{12}\frac{RB_\varphi}{f},$$

$$A(6,3) = hh\cdot g_{22}\frac{RB_\varphi}{f},$$

$$A(6,6) = hh\cdot\frac{-R^2}{fJ}\left[\mathrm{i}m'\chi'\frac{g_{22}}{\rho_0J} + \mathrm{i}ng_{22}\frac{V_\varphi}{R} + \eta\left(\frac{n^2}{R^2}g_{22} + mm'\right)\right],$$

$$A(6,7) = hH'\cdot\frac{R^2}{fJ}\left(\mathrm{i}\chi'\frac{g_{22}}{\rho_0J} + m\eta\right) + hH\cdot ng_{12}\frac{R^2}{fJ}\left(-\frac{V_\varphi}{R} + \frac{\mathrm{i}n}{R^2}\eta\right),$$

$$A(6,8) = hH'\cdot\frac{R^2}{fJ}g_{22}\left(\mathrm{i}\frac{V_\varphi}{R} + \frac{n}{R^2}\eta\right) + hH\cdot\frac{R^2}{fJ}m'g_{12}\left(\frac{V_\varphi}{R} - \mathrm{i}\frac{n}{R^2}\eta\right),$$

$$A(7,2) = HH\cdot\frac{-RB_\varphi}{f}g_{11},$$

$$A(7,3) = Hh\cdot\frac{RB_\varphi}{f}\mathrm{i}g_{12},$$

$$A(7,6) = H'h \cdot \frac{R^2}{fJ}\eta m' + Hh \cdot \frac{R^2}{fJ} g_{12}\left(\chi' m' \frac{1}{\rho_0 J} + n\frac{V_\varphi}{R} - \mathrm{i}\frac{n^2}{R^2}\eta\right),$$

$$A(7,7) = H'H' \cdot \frac{-\eta R^2}{fJ} + HH' \cdot \frac{-\chi'}{f}\frac{g_{12}}{\rho_0 J}\frac{R^2}{J} + HH \cdot -n g_{11}\frac{R^2}{fJ}\left(\mathrm{i}\frac{V_\varphi}{R} + \frac{n}{R^2}\eta\right),$$

$$A(7,8) = HH' \cdot g_{12}\frac{R^2}{fJ}\left(-\frac{V_\varphi}{R} + \frac{\mathrm{i}n}{R^2}\eta\right) + HH \cdot m' g_{11}\frac{R^2}{fJ}\left(\mathrm{i}\frac{V_\varphi}{R} + \frac{n}{R^2}\eta\right),$$

$$A(8,2) = HH \cdot \frac{fJ}{R^2},$$

$$A(8,6) = H'h \cdot n\frac{\eta}{f}\frac{g_{22}}{J} + Hh \cdot \mathrm{i}mn\frac{\eta}{f}\frac{g_{12}}{J},$$

$$A(8,7) = H'H \cdot -\mathrm{i}n\frac{\eta}{f}\frac{g_{12}}{J} + HH \cdot n\left(\mathrm{i}f\chi'\frac{1}{\rho_0 R^2} + m\frac{\eta}{f}\frac{g_{11}}{J}\right),$$

$$A(8,8) = H'H' \cdot -\frac{\eta}{f}\frac{g_{22}}{J} + H'H \cdot \mathrm{i}m'\frac{\eta}{f}\frac{g_{12}}{J} + HH' \cdot -\mathrm{i}m\frac{\eta}{f}\frac{g_{12}}{J} + HH \cdot -m'\left(\mathrm{i}f\chi'\frac{1}{\rho_0 R^2} + m\frac{\eta}{f}\frac{g_{11}}{J}\right).$$

References

[2] A.J.C. Beliën, M.A. Botchev, J.P. Goedbloed, B. van der Holst, R. Keppens, J. Comp. Phys. 182 (2002) 91.
[3] A. Bondeson, R. Iacono, A. Bhattacharjee, Phys. Fluids 30 (1987) 2167.
[4] A. Bondeson, G. Vlad, H. Lütjens, Controlled fusion and plasma heating, in: Proceedings of the 17th European Conference, Amsterdam, The Netherlands (European Physical Society, Petit-Lancy, 1990) B Part II 14, 1990, p. 906.
[5] A. Bondeson, G. Vlad, H. Lütjens, Phys. Fluids B 4 (1992) 1889.
[7] C. Busch, in: Proceedings of 32nd EPS Conference on Plasma Physics, ECA VCol C, vol. 29, 2005, P-1.016.
[8] D. Chandra, A. Sen, P. Kaw, M.P. Bora, S. Kruger, Nucl. Fusion 45 (2005) 524.
[9] C.Z. Cheng, M.S. Chance, J. Comp. Phys. 71 (1987) 124.
[10] K. Crombé et al., Phys. Rev. Lett. 95 (2005) 155003.
[12] J.P. Goedbloed, Physica 53 (1971) 501.
[13] J.P. Goedbloed, Phys. Fluids 18 (1975) 1258.
[14] J.P. Goedbloed, Space Sci. Rev. 107 (2003) 353.
[15] J.P. Goedbloed, Phys. Scripta T 107 (2004) 159.
[16] J.P. Goedbloed, A.J.C. Beliën, B. van der Holst, R. Keppens, AIP Conf. Proc. 703 (2004) 42.
[17] J.P. Goedbloed, A.J.C. Beliën, B. van der Holst, R. Keppens, Phys. Plasmas 11 (2004) 28.
[18] J.P. Goedbloed, A.J.C. Beliën, B. van der Holst, R. Keppens, Phys. Plasmas 11 (2004) 4332.
[20] J.P. Goedbloed, P.H. Sakanaka, Phys. Fluids 17 (1974) 908.
[21] G.H. Golub, C.F. van Loan, Matrix Computations, third ed., The Johns Hopkins University Press, Baltimore, MD, 1996.
[22] H. Grad, H. Rubin, in: Proceedings of the Second UN International Conference on the Peaceful Uses of Atomic Energy, vol. 31, 1958, p. 190.
[23] R.C. Grimm, J.M. Greene, J.L. Johnson, Methods Comput. Phys. 16 (1976) 253.
[24] R. Gruber, J. Rappaz, Finite Element Methods in Linear Ideal Magnetohydrodynamics, Springer, New York, 1985.
[25] R. Gruber, F. Troyon, D. Berger, L.C. Bernard, S. Rousset, R. Schreider, W. Kerner, W. Schneider, K.V. Roberts, Comp. Phys. Commun. 21 (1981) 323.
[26] L. Guazzotto, R. Betti, J. Manickham, S. Kaye, Phys. Plasmas 11 (2004) 604.
[27] K. Hain, R. Lüst, Z. Naturforsch. 13a (1958) 936.
[28] E. Hameiri, Ph.D. thesis, New York University, 1976.
[29] E. Hameiri, Phys. FLuids 26 (1983) 230.
[30] S.P. Hirshman, Nucl. Fusion 18 (1978) 917.
[31] B. van der Holst, A.J.C. Beliën, J.P. Goedbloed, Phys. Rev. Lett. 84 (2000) 2865.
[32] B. van der Holst, A.J.C. Beliën, J.P. Goedbloed, Phys. Plasmas 7 (2000) 4208.
[33] C.T. Hsu, K.C. Shaing, R. Gormley, Phys. Plasmas 1 (1996) 132.
[34] G.T.A. Huysmans, J.P. Goedbloed, W. Kerner, in: Proceedings of CP90 Conf. on Comp. Phys. Proc., 1991, p. 371.
[35] G.T.A. Huysmans, J.P. Goedbloed, W. Kerner, Phys. Fluids B 5 (1993) 1545.
[36] R. Keppens, F. Casse, J.P. Goedbloed, ApJ 569 (2002) L121.
[37] W. Kerner, J.P. Goedbloed, G.T.A. Huysmans, S. Poedts, E. Schwarz, J. Comput. Phys. 142 (1998) 271.
[38] R.C. Morris, M.G. Haines, R.J. Hastie, Phys. Plasmas 3 (1996) 4513.
[39] M. Nool, A. van der Ploeg, SIAM J. Sci. Comput. 22 (2000) 95.
[40] Y.P. Pao, Nucl. Fusion 15 (1975) 631.

[41] S. Poedts, W. Kerner, Phys. Rev. Lett. 66 (1991) 2871.
[42] S. Poedts, E. Schwarz, J. Comp. Phys. 105 (1993) 165.
[43] J. Rappaz, Numer. Math. 28 (1977) 15.
[44] Y. Saad, M.H. Schultz, SIAM J. Sci. Stat. Comput. 7 (1986) 856.
[45] S. Semenzato, R. Gruber, H.P. Zehrfeld, Comput. Phys. Rep. 1 (1984) 389.
[46] V.D. Shafranov, Sov. Phys. JETP 6 (1958) 545.
[47] K.C. Shaing, S.P. Hirshman, Phys. Fluids B 1 (1989) 705.
[48] G.L.G. Sleijpen, H.A. van der Vorst, SIAM J. Matrix Anal. Appl. 17 (1996) 401.
[49] L.S. Soloviev, Sov. Phys. JETP 26 (1968) 400.
[50] T.H. Stix, Phys. Fluids 16 (1973) 1260.
[51] G. Strang, G.J. Fix, Analysis of the finite element method, Prentice Hall, Englewood, NJ, 1973.
[52] E. Strumberger, S. Günter, P. Merkel, S. Riondato, E. Schwarz, C. Tichmann, H.P. Zehrfeld, Nucl. Fusion 45 (2005) 1156.
[53] M. Taguchi, Phys. Plasmas Control Fusion 33 (1991) 859.
[54] H.P. Zehrfeld, B.J. Green, Nucl. Fusion 12 (1972) 569.
[55] R. Zelazny, R. Stankiewicz, A. Galkowski, S. Potempski, Plasma Phys. Control Fusion 35 (1993) 1215.